

Determination of parafoil lift and drag coefficients using both
three-dimensional modeling and experimental methods

by

Joshua Aaron Bowman

A thesis submitted to the graduate faculty
in partial fulfillment of the requirements for the degree of
MASTER OF SCIENCE

Major: Aerospace Engineering

Program of Study Committee:
Frederick L. Haan Jr., Major Professor
Jerald M. Vogel
John P. Basart

Iowa State University

Ames, Iowa

2004

Copyright © Joshua Aaron Bowman, 2004. All rights reserved.

Graduate College
Iowa State University

This is to certify that the master's thesis of
Joshua Aaron Bowman
has met the thesis requirements of Iowa State University

Signatures have been redacted for privacy

DEDICATION

I would like to dedicate this thesis to my parents Donald and Nancy Bowman, and to Tamyra who is a light in my life. I would also like to thank my friends and family without their advice and support this work would not have been possible.

TABLE OF CONTENTS

LIST OF TABLES	vi
LIST OF FIGURES	vii
NOMENCLATURE	ix
ABSTRACT	xiii
CHAPTER 1. INTRODUCTION	1
1.1 Background	1
1.2 Past Research	1
1.3 Current Work	2
CHAPTER 2. PARAFOIL EQUATIONS OF MOTION	3
2.1 Rigid Body Equations	3
2.2 Euler's Equation of Motion	5
2.3 Coordinate Transformation	7
2.4 Apparent Mass Effects	10
2.5 Developing the State Matrix	12
CHAPTER 3. AERODYNAMIC ANALYSIS PROCEDURES	14
3.1 Two Dimensional Lifting Line Theory	14
3.2 Panel Method Analysis	18
3.3 Wind Fan Bank	20
3.4 Drop Test Experiment	22

CHAPTER 4. RECOVERY GUIDANCE SYSTEM EQUIPMENT . . .	28
4.1 Cut Down Box	28
4.2 Differential Global Positioning System	29
4.3 Control Line Servomechanism	30
4.4 Parafoil Strings	31
CHAPTER 5. RESULTS AND DISCUSSION	33
5.1 Lifting Line Data	33
5.2 PMARC Results	35
5.3 Comparison of PMARC Values to Lifting Line Theory	37
5.4 Experimental Results	40
5.5 Comparison of Experimental Data to Theoretical Values	41
CHAPTER 6. CONCLUSIONS AND FUTURE WORK	43
APPENDIX A. PMARC AIRFOILS	45
APPENDIX B. AIRFOIL INPUT GEOMETRY FOR PMARC	53
APPENDIX C. UNCERTAINTY ANALYSIS	57
C.1 Precision Error	57
C.2 Bias Error	58
BIBLIOGRAPHY	63
ACKNOWLEDGMENTS	65

LIST OF TABLES

Table 5.1	Common constants in lifting line analysis	33
Table 5.2	Results from experimental drops	40
Table 5.3	Comparison of C_L data of improved PMARC airfoil with exper- imental data	41
Table 5.4	Comparison of C_D data of PMARC with experimental data . . .	42
Table B.1	The PMARC panels input without tapering	54
Table B.2	The PMARC panels input with tapering for upper surface	55
Table B.3	The PMARC panels input with tapering for lower surface	56
Table C.1	Uncertainty of Drop One	62

LIST OF FIGURES

Figure 2.1	Parafoil orientation from Etkins (1)	8
Figure 3.1	Illustration of parafoil geometry including the anhedral angle defined as β	16
Figure 3.2	Overlay of created airfoil with parafoil	19
Figure 3.3	PMARC airfoil at angle of incidence of 3 degrees	20
Figure 3.4	Wind fan bank used for lift and drag estimates with the parafoil	21
Figure 3.5	Full configuration of balloon experiments	23
Figure 3.6	A frame from video to illustrate drop distance estimation procedures	24
Figure 3.7	Illustration defining glide slope angle and angle of incidence for the parafoil	25
Figure 3.8	Parameters of the glide slope of the parafoil	26
Figure 4.1	Differential Global Positioning board	30
Figure 4.2	Memory Module for data from the DGPS system	30
Figure 4.3	Control line servomechanism	31
Figure 4.4	Parafoil string configuration	32
Figure 5.1	Lift coefficient as a function of angle of incidence	34
Figure 5.2	Drag coefficient as a function of angle of incidence	35
Figure 5.3	Lift coefficient as a function of angle of incidence	36

Figure 5.4	Drag coefficient as a function of angle of incidence	37
Figure 5.5	Lift coefficient as a function of rigging angle	38
Figure 5.6	Drag coefficient as a function of rigging angle	39
Figure A.1	Pressure distribution results calculated from PMARC for the air- foil at an angle of incidence of -10 degrees	45
Figure A.2	Pressure distribution results calculated from PMARC for the air- foil at an angle of incidence of -5 degrees	46
Figure A.3	Pressure distribution results calculated from PMARC for the air- foil at an angle of incidence of zero degrees	47
Figure A.4	Pressure distribution results calculated from PMARC for the air- foil at an angle of incidence of 3 degrees	48
Figure A.5	Pressure distribution results calculated from PMARC for the air- foil at an angle of incidence of 5 degrees	49
Figure A.6	Pressure distribution results calculated from PMARC for the air- foil at an angle of incidence of 10 degrees	50
Figure A.7	Pressure distribution results calculated from PMARC for the air- foil at an angle of incidence of 15 degrees	51
Figure A.8	Pressure distribution results calculated from PMARC for the air- foil at an angle of incidence of 20 degrees	52

NOMENCLATURE

Lower case

a	lift curve for a wing ($\frac{\text{lift}}{\text{angle of incidence}}$)
a_o	two dimensional lift curve slope ($\frac{\text{lift}}{\text{angle of incidence}}$)
a'_o	two dimensional lift curve slope adjusted for small aspect ratio ($\frac{\text{lift}}{\text{angle of incidence}}$)
ρ	ambient density ($\frac{lbs_m}{ft^3}$)
g_o	gravitational constant ($g_o = 32.2 \frac{ft}{second^2}$)
t	time (<i>seconds</i>)
b	constructed span of parafoil (ft^2)
s	area of parafoil (ft^2)
$arch$	parafoil span wise arch angle (<i>degrees</i>)
c	chord of the parafoil (ft)
α	angle of incidence (<i>degrees</i>)
m	mass (<i>lbs</i>)
v_c	velocity vector of vehicle mass center ($\frac{ft}{second}$)
α_{zl}	zero lift angle of incidence (<i>degrees</i>)

r	distance from the parafoil to landing site (ft)
h	angular momentum $\frac{ft^2}{second}$
ih	parafoil inlet height ($inches$)
n	number of lines
d	diameter of lines ($inches$)
q_∞	dynamic pressure ($\frac{lb_m}{ft \cdot second^2}$)
ω	angular velocity ($\frac{degrees}{second}$)
α	angle of attack ($degrees$)
ϵ	side slip angle ($degrees$)
λ	a small positive factor for minimum elliptical loading

Upper case

C_L	coefficient of lift
C_D	coefficient of drag
β	anhedral angle ($degrees$)
\vec{F}	resultant external force vector
\vec{G}	resultant external moment vector
U, V, W	scalar components of V_c $\frac{ft}{second}$
Q, R, P	roll, pitch, and yaw rate $\frac{degrees}{second}$
L, M, N	scalar components of G

Φ	Euler angle roll (<i>degrees</i>)
Ψ	Euler angle pitch (<i>degrees</i>)
Θ	Euler angle yaw (<i>degrees</i>)
T_1	standard atmosphere temperature (<i>Rankin</i>)
T	measured temperature (<i>Rankin</i>)
P_1	standard atmosphere pressure ($\frac{lbs}{ft^2}$)
P	calculated pressure ($\frac{lbs}{ft^2}$)
\mathcal{R}	aspect ratio
R_g	gas constant ($\frac{(ft)(lbs)}{(slug)(R)}$)
V_T	total velocity ($\frac{ft}{second^2}$)
I_A, I_B, I_C	moment of inertia for the parafoil $\frac{ft^2}{lb_m}$
J_X, J_Y, J_Z	moment of inertia for the payload $\frac{ft^2}{lb_m}$
SP	area of payload (ft^2)
R	mean line length (<i>inches</i>)
L	lift (<i>lbs</i>)
D	drag (<i>lbs</i>)
M	moment (<i>lbs</i>)
wt	weight (lbs_m)

Acronyms

RGS	Recovery Guidance System
HABET	High Altitude Ballooning Experiments in Technology
SPADES	Small Parafoil Autonomous Delivery System
SSOL	Spacecraft Systems and Operations Laboratory

ABSTRACT

The High Altitude Balloon Experiments in Technology (HABET) program started at Iowa State University to carry payloads into the upper atmosphere and to simulate the activities involved with satellite programs. As HABET has evolved through the years the payloads for HABET have become increasingly more sophisticated and expensive. The current recovery system employs a circular parachute that does not provide any means of control. This allows the payload to land in inconvenient locations such as roads or train tracks. The parachute can also land in places where the payload is not recoverable such as lakes or rivers, even causing injury to people, property or animals. The Recovery Guidance System (RGS) is a solution to these problems. The goal of the Recovery Guidance System project is to develop a fully autonomous landing system that will select its landing sites from a list of preprogrammed sites based on where the system is and where it can go. This research is designed to give the RGS project a better understanding of the aerodynamic properties of the parafoil. This research has three parts. First, a two dimensional lifting line equation is used to determine the lift coefficient and the drag coefficient. Next, a three dimensional model of the parafoil used in the RGS program was put into a program called PMARC to obtain the coefficients of lift and drag. Finally, the parafoil was hooked up to a dummy payload of the same size and weight as the RGS electronic package so that the coefficient of lift and drag were experimentally obtained. All of these results were then compared to each other for accuracy. The lift coefficient values were close to the predicted values (± 16 percent) but the predicted drag coefficient values differed from the experimental results by a factor

of three.

CHAPTER 1. INTRODUCTION

1.1 Background

The High Altitude Ballooning Experiments in Technology (HABET) was formed in 1995 at Iowa State University to launch payloads into the upper atmosphere and to give students a background in satellite activities. As more and more sophisticated and expensive payloads were launched the need for a more controlled means of recovery became apparent. Currently, the landing device used is a circular parachute that is uncontrollable. This can cause two major problems. The first problem is that the payload can cause injury or property damage where it lands. The second is that the payload can land in a location that is not recoverable such as a lake or a river. The Recovery Guidance System (RGS) project was started to overcome these problems.

1.2 Past Research

The idea of a recovery guidance platform is not a new one. In fact the Netherlands Dutch Space Program in partnership with the National Aerospace Laboratory of France is developing a cargo delivery system called SPADES (Small Parafoil Autonomous Delivery System). This system is designed to carry payloads from 100-200kg to a designated landing site. One of the technical requirements of HABET and a large design difference between RGS and SPADES is that HABET payloads are 1-10 kg. The RGS project at Iowa State University was begun by John Bendle, a Graduate student at Iowa State

University in 1997. John Bendle started the project by designing a fuzzy logic controller for an automated payload return system. In 1999, the project was then taken over by Bruce Tsai. His work involved using a vortex lattice flow field to estimate the aerodynamic coefficients (C_L and C_D) of the parafoil and then design a proportional navigation controller from these coefficients.

1.3 Current Work

The next stage in the project was to expand and verify Bruce Tsai's work by first calculating the coefficient of lift (C_L) and the coefficient of drag (C_D) by using a two dimensional lifting line theory, and using a three dimensional modeling code called PMARC to get the aerodynamic coefficients of lift and drag. The final step in this project was to verify the theoretical calculation by experimentally determining the coefficients of lift and drag using the parafoil itself at the angles of incidence of three degrees and ten degrees.

CHAPTER 2. PARAFOIL EQUATIONS OF MOTION

Before a control system can be implemented, the fundamental dynamics of the system must be understood. In the case of the Recovery Guidance System, this means the ram air parafoil aerodynamics. This is begun by developing the equations of motion for a ram air parafoil. The equations of motion are derived by the method outlined in Etkins (1). For the analysis, rigid body dynamics are assumed. Also assumed is that the earth is flat and stationary in inertial space.

2.1 Rigid Body Equations

The analysis begins by developing the rigid-body equations using Newton's second law to define an elemental mass of the vehicle, ∂m , having a velocity \vec{v} relative to the inertial axes and a resultant force, $\partial \vec{F}$, acting on it. Doing this the following reveals equation:

$$\partial \vec{F} = \partial m \cdot \frac{d\vec{v}}{dt} \quad (2.1)$$

When all the elemental masses of the vehicle are summed together it yields

$$\sum \partial \vec{F} = \sum \partial m \cdot \frac{d\vec{v}}{dt} = \frac{d}{dt} \sum \vec{v} \partial m \quad (2.2)$$

The summation, $\sum \partial \vec{F}$ represents all the forces acting on the elemental masses including internal forces. These internal forces are canceled out by Newton's third law. This simplifies the equation to $\sum \partial \vec{F} = \vec{F}$ Next, consider the velocity vector represented by:

$$\vec{v} = \vec{v}_c + \frac{d\vec{r}}{dt} \quad (2.3)$$

Where \vec{v}_c is the velocity at the center of mass. Summing up all the velocity vectors gives us:

$$\sum \vec{v} \partial m = \sum (\vec{v}_c + \frac{d\vec{r}}{dt}) \partial m = m \vec{v}_c + \frac{d}{dt} \sum \vec{r} \partial m \quad (2.4)$$

Since $\sum \vec{r} \cdot \partial m = 0$ (at the center of gravity), equation 2.4 reduces to:

$$\sum \vec{v} \partial m = m \cdot \vec{v}_c \quad (2.5)$$

Finally, equation 2.1 becomes :

$$\vec{F} = m \frac{d\vec{v}_c}{dt} \quad (2.6)$$

The next step is to establish a relationship between the external moment and the rotation of the parafoil.

$$\sum \tau = \frac{d}{dt}(\partial \vec{h}) = \frac{d}{dt}(\vec{r} \times \vec{v}) \partial m = \frac{d\vec{r}}{dt} \times \vec{v} \partial m + \vec{r} \times \frac{d\vec{v}}{dt} \partial m \quad (2.7)$$

Where \vec{h} is the angular momentum. Rearranging Equation 2.3 you get:

$$\frac{d\vec{r}}{dt} = \vec{v} - \vec{v}_c \quad (2.8)$$

Using the moment of $\partial \vec{F}$ about the center of mass of the system transform Equation into 2.7

$$\partial \vec{G} = \frac{d}{dt}(\partial \vec{h}) - (\vec{v} - \vec{v}_c) \times \vec{v} \partial m \quad (2.9)$$

Where ∂G is the moment of ∂F about C . Summing all the elements Equation 2.9 reduces down to:

$$\sum \partial \vec{G} = \frac{d}{dt} \sum (\partial \vec{h}) + \vec{v}_c \times \sum \vec{v} \partial m \quad (2.10)$$

Combining Equation 2.5 and $\vec{v}_c \times \vec{v}_c = 0$, Equation 2.10 reduces to:

$$\vec{G} = \frac{d\vec{h}}{dt} \quad (2.11)$$

Equations 2.6 and 2.11 are known as the two vector equations of motion that represent the force and moment equations of the vehicle.

2.2 Euler's Equation of Motion

In Equation 2.11 the derivatives are taken with respect to time. If the reference axes are non-rotating then as the vehicle rotates the moments and products of inertia will vary with time. This is a very undesirable condition that will be overcome by fixing the reference frame of $Cxyz$ to the vehicle. The origin O is assumed to coincide with C at $t = 0$. To fix the reference frame, consider the derivative of vector, \vec{A} , in a frame of reference rotating with an angular velocity ω :

$$\frac{d\vec{A}}{dt} = \frac{\partial \vec{A}}{\partial t} + \omega \times \vec{A} \quad (2.12)$$

Applying Equation 2.12 to Equation 2.1 and Equation 2.11 shows that

$$\vec{F} = m \cdot \frac{\partial \vec{v}_c}{\partial t} + m \cdot \vec{\omega} \times \vec{v}_c \quad (2.13)$$

$$\vec{G} = \frac{\partial \vec{h}}{\partial t} + \vec{\omega} \times \vec{h} \quad (2.14)$$

Expanding equations 2.13 and 2.14 into their scalar components gives the equations:

$$\begin{aligned}
 F_x &= m(\dot{U} + QW - RV) \\
 F_y &= m(\dot{V} + RU - PW) \\
 F_z &= m(\dot{W} + PV - QU)
 \end{aligned} \tag{2.15}$$

where U , V , and W are the velocity components of x, y, z respectively, and Q , R , and P are the roll, pitch, and yaw rates respectively.

$$\begin{aligned}
 L &= \dot{h}_x + Qh_z - Rh_y \\
 M &= \dot{h}_y + Rh_x - Ph_z \\
 N &= \dot{h}_z + Ph_y - Qh_x
 \end{aligned} \tag{2.16}$$

where L , M , and N are the scalar components of the external moment vector G .

The variables α (the angle of attack), ϵ (side slope angle), and V_T (total velocity) can then be expressed in terms of the velocity components by the Equations:

$$\begin{aligned}
 \tan \alpha &= \frac{W}{U} \\
 \sin \epsilon &= \frac{V}{V_T} \\
 V_T &= \sqrt{U^2 + V^2 + W^2}
 \end{aligned} \tag{2.17}$$

and:

$$\begin{aligned}
 \dot{\alpha} &= \frac{U \cdot \dot{W} - W \cdot \dot{U}}{U^2 - W^2} \\
 \dot{\epsilon} &= \frac{\dot{V} \cdot V_T - V \cdot \dot{V}_T}{V_T^2 \cos \epsilon} \\
 \dot{V}_T &= U \cdot \dot{U} + V \cdot \dot{V} + W \cdot \dot{W} V_T
 \end{aligned} \tag{2.18}$$

2.3 Coordinate Transformation

Since the Euler Equations are for a fixed reference frame, to be of any analytical value to this analysis the equations must be transformed into an earth fixed reference frame of $ox'y'z'$ as shown in Figure 2.1.

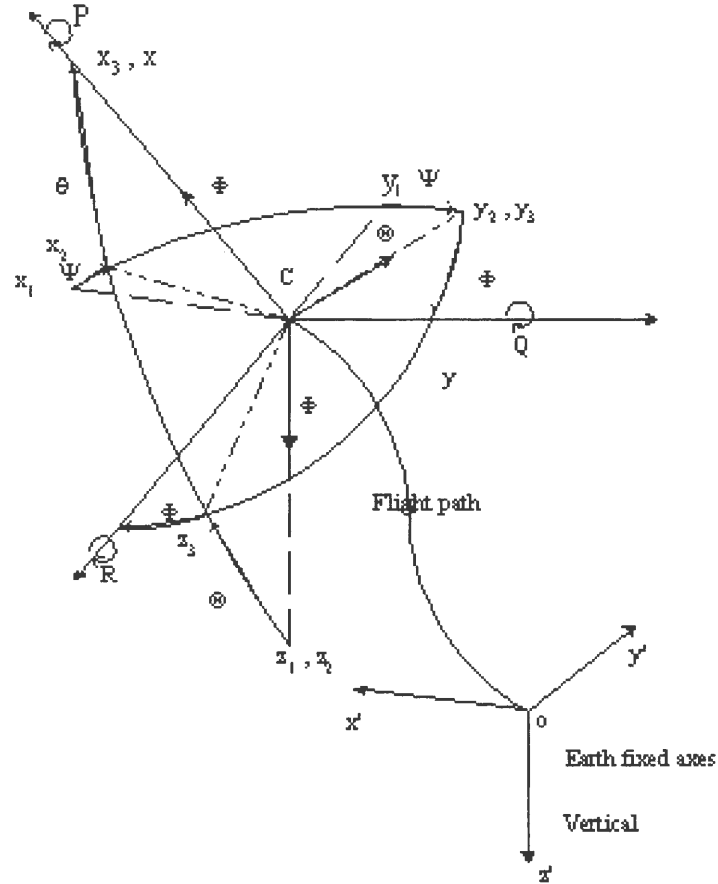


Figure 2.1 Parafoil orientation from Etkins (1)

To relate the parafoil's orientation to an earth fixed frame of reference, a series of coordinate transformations must be enacted. The parafoil is assumed to be oriented so that its axes are parallel to $ox'y'z'$ so that the parafoil is in position $Cx_1y_1z_1$. Then the following transformations are applied. First a rotation of angle Ψ about oz_1 , carrying the axes to $Cx_2y_2z_2$. This rotation will take the form:

$$\begin{bmatrix} \hat{i}_1 \\ \hat{j}_1 \\ \hat{k}_1 \end{bmatrix} = \begin{bmatrix} \cos \Psi & -\sin \Psi & 0 \\ \sin \Psi & \cos \Psi & 0 \\ 0 & 0 & 1 \end{bmatrix} \cdot \begin{bmatrix} \hat{i}_2 \\ \hat{j}_2 \\ \hat{k}_2 \end{bmatrix} \quad (2.19)$$

The next transformation will be the rotation of angle Θ about oy_2 carrying the axes to $Cx_3y_3z_3$ as shown in matrix 2.20:

$$\begin{bmatrix} \hat{i}_2 \\ \hat{j}_2 \\ \hat{k}_2 \end{bmatrix} = \begin{bmatrix} \cos \Theta & 0 & \sin \Theta \\ 0 & 1 & 0 \\ -\sin \Theta & 0 & \cos \Theta \end{bmatrix} \cdot \begin{bmatrix} \hat{i}_3 \\ \hat{j}_3 \\ \hat{k}_3 \end{bmatrix} \quad (2.20)$$

The final transformation will be a rotation of angle Φ about ox_3 carrying the axes to the final position of $Cxyz$ as shown in matrix 2.21:

$$\begin{bmatrix} \hat{i}_3 \\ \hat{j}_3 \\ \hat{k}_3 \end{bmatrix} = \begin{bmatrix} 1 & 0 & 0 \\ 0 & \cos \Phi & -\sin \Phi \\ 0 & \sin \Phi & \cos \Phi \end{bmatrix} \cdot \begin{bmatrix} \hat{i} \\ \hat{j} \\ \hat{k} \end{bmatrix} \quad (2.21)$$

Putting all these transformations together results in the matrix:

$$\begin{bmatrix} \dot{x}' \\ \dot{y}' \\ \dot{z}' \end{bmatrix} = \begin{bmatrix} \cos \Theta \cos \Psi & \sin \Phi \sin \Theta \cos \Psi - \cos \Phi \sin \Psi & \cos \Phi \sin \Theta \cos \Phi + \sin \Phi \sin \Psi \\ \cos \Theta \sin \Psi & \sin \Phi \sin \Theta \sin \Psi + \cos \Phi \cos \Psi & \cos \Phi \sin \Theta \sin \Phi - \sin \Phi \cos \Psi \\ -\sin \Theta & \sin \Phi \cos \Theta & \cos \Phi \cos \Theta \end{bmatrix} \cdot \begin{bmatrix} U \\ V \\ W \end{bmatrix} \quad (2.22)$$

Now that this transformation has been laid out, the velocity components of the parafoil can be expressed as:

$$\begin{aligned}
\dot{x}' &= U \cdot \cos \Theta \cos \Psi + V \cdot (\sin \Phi \sin \Theta \cos \Psi - \cos \Phi \sin \Psi) + W \cdot (\cos \Phi \sin \Theta \cos \Psi + \sin \Theta \sin \Psi) \\
\dot{y}' &= U \cdot \cos \Theta \sin \Psi + V \cdot (\sin \Phi \sin \Theta \sin \Psi + \cos \Phi \sin \Psi) + W \cdot (\cos \Phi \sin \Theta \sin \Psi - \sin \Theta \cos \Psi) \\
\dot{z}' &= -U \cdot \sin \Theta + V \cdot \sin \Phi \cos \Theta + W \cdot \cos \Psi \cos \Theta
\end{aligned} \tag{2.23}$$

these equations are called the navigation equations. Similarly the yaw, pitch, and roll rate can go through the coordinate transformation and be expressed as:

$$\begin{aligned}
\dot{\Theta} &= Q \cos \Phi - R \sin \Phi \\
\dot{\Phi} &= P + Q \sin \Phi \tan \Theta + R \cos \Phi \tan \Theta \\
\dot{\Psi} &= (Q \sin \Phi + R \cos \Phi) \cdot \Theta
\end{aligned} \tag{2.24}$$

these equations are called the kinematic equations.

2.4 Apparent Mass Effects

Apparent mass effects must also be added to the analysis of the parafoil. Apparent mass effects are the result of external forces of the fluid acting on the vehicle as the vehicle travels through the fluid. Apparent mass effects are most relevant on lightly loaded vehicles such as a parafoil. Just as apparent moments of inertia are seen in rotational equations, the apparent mass effects become apparent in aerodynamic angles and the true velocity. The calculation of these effects are outlined in Lissman and Brown (6) and are shown in equations 2.25 and 2.26.

$$\begin{aligned}
m_x &= 0.666 \cdot \rho \cdot t^2 \cdot b \\
m_y &= 0.267 \cdot \rho \cdot t^2 \cdot c \\
m_z &= \frac{0.785 \cdot \rho \cdot b \cdot c \cdot \mathcal{R}}{1 + \mathcal{R}}
\end{aligned} \tag{2.25}$$

$$\begin{aligned}
I_A &= \frac{0.055 \cdot \rho \cdot \mathcal{R} \cdot b \cdot s^2}{1 + \mathcal{R}} \\
I_B &= \frac{0.038 \cdot \rho \mathcal{R}}{1 + \mathcal{R}} \left[1 + \frac{\pi}{6} (1 + \mathcal{R}) \mathcal{R} \cdot arch^2 \cdot t^2 \right] \cdot c^3 \cdot S \\
I_C &= \frac{0.0308 \cdot \rho \cdot \mathcal{R}}{1 + \mathcal{R}} \left[1 + \frac{\pi}{6} (1 + \mathcal{R}) \mathcal{R} \cdot arch^2 \cdot t^2 \right] \cdot c^3 \cdot S
\end{aligned} \tag{2.26}$$

Where \mathcal{R} is the aspect ratio and $arch$ is the span wise arch angle. Applying the apparent mass effects to the forces on the parafoil reveals equation 2.27:

$$\begin{aligned}
\dot{\alpha} &= \frac{-F_T \cdot \sin \alpha - L + (m + m_x) \cdot V_T \cdot Q + (m + m_x) \cdot g \cdot XX}{(m + m_x) \cdot V_T \cdot \cos \beta} \\
\dot{\epsilon} &= \frac{-F_T \cdot \cos \alpha + Y + (m + m_x) \cdot V_T \cdot R + (m + m_x) \cdot g \cdot YY}{(m + m_y) \cdot V_T} \\
\dot{V}_T &= \frac{F_T \cdot \cos \alpha - D + (m + m_x) \cdot V_T + (m + m_x) \cdot g \cdot ZZ}{(m + m_x)}
\end{aligned} \tag{2.27}$$

where:

$$\begin{aligned}
XX &= (\sin \alpha \sin \Theta + \cos \alpha \cos \Phi \cos \Theta) \\
YY &= (\cos \alpha \sin \beta \sin \Theta + \cos \beta \sin \Phi \cos \Theta - \sin \alpha \sin \beta \cos \Phi \cos \Theta) \\
ZZ &= (-\cos \alpha \cos \beta \sin \Theta + \sin \beta \sin \Phi \cos \Theta + \sin \alpha \cos \beta \sin \Theta + \sin \beta \sin \Phi \cos \Theta + \sin \alpha \cos \beta \cos \Phi \cos \Theta)
\end{aligned} \tag{2.28}$$

these equations are called the force equations. Applying the apparent mass effects to the roll, pitch, and yaw rate of the parafoil reveals equation 2.29. These equations are also called the moment equations.

$$\begin{aligned}
\dot{P} &= \frac{(L_{RM} - Q \cdot R \cdot J_z + Q \cdot R \cdot J_y)}{J_x + I_A} \\
\dot{Q} &= \frac{(M_{pm} - P \cdot R \cdot J_x + P \cdot R \cdot J_z)}{J_y + I_B} \\
\dot{R} &= \frac{(N_{ym} - P \cdot Q \cdot J_x + P \cdot Q \cdot J_z)}{J_z + I_C}
\end{aligned} \tag{2.29}$$

2.5 Developing the State Matrix

Combining the equation sets 2.15, 2.16, 2.24, and 2.23 gives us the equations of motion for the parafoil with six degrees of freedom. The current configuration of the ram air parafoil setup does not have any thrust. Since the parafoil has no means of thrust it does not have any control over the z , up-down, direction. Therefore in this analysis the term of F_T is removed also it is assumed that $\Phi = 0$ and $\Psi = 0$ (no rolling or yaw). Removing these terms and regrouping the equations into more manageable terms gives the equations of motion for the parafoil as:

$$\begin{aligned}
\dot{V}_T &= \frac{-D - (m + m_x) \cdot g \cdot \sin(\Theta - \alpha)}{(m + m_x)} \\
\dot{\alpha} &= \frac{-L + (m + m_x) \cdot g \cdot \cos(\Theta - \alpha)}{(m + m_x) \cdot V_T} + Q \\
\dot{\Theta} &= Q \\
\dot{Q} &= \frac{M}{J_y + I_B} \\
\dot{x}' &= V_T \cdot \cos(\Theta - \alpha) = \dot{U} \\
\dot{z}' &= V_T \cdot \sin(\Theta - \alpha) = \dot{W}
\end{aligned} \tag{2.30}$$

Expanding D, L and M that relates to α and δ_f .

$$\begin{aligned}
 D &= (C_{D\alpha}\alpha + C_{D\delta_f}\delta_f) \cdot q_\infty \cdot S \\
 L &= (C_{L\alpha}\alpha + C_{L\delta_f}\delta_f) \cdot q_\infty \cdot S \\
 M &= (C_{M0} + C_{M\alpha}\alpha + C_{M\delta_f}\delta_f) \cdot q_\infty \cdot S
 \end{aligned} \tag{2.31}$$

where δ_f is the flap deflection, D , L , and M is the drag, lift and moment of the parafoil respectively.

Now that the equations of motion for the parafoil have been derived, the state matrix can be set up. The state matrix will predict the motions of the parafoil, or what state the parafoil is in any point in time. In this design only four states on the parafoil are of interest: the parafoil's acceleration in the x direction and the z direction and the derivatives of the pitch angle and the pitch rate. To find the state matrix the partial derivatives of the scalar velocities (U, W) the pitch rate and the pitch angle are combined together as shown by the matrix 2.32

$$\begin{bmatrix}
 \frac{\partial \dot{U}}{\partial U} & \frac{\partial \dot{U}}{\partial W} & \frac{\partial \dot{U}}{\partial Q} & \frac{\partial \dot{U}}{\partial \Theta} \\
 \frac{\partial \dot{W}}{\partial U} & \frac{\partial \dot{W}}{\partial W} & \frac{\partial \dot{W}}{\partial Q} & \frac{\partial \dot{W}}{\partial \Theta} \\
 \frac{\partial \dot{Q}}{\partial U} & \frac{\partial \dot{Q}}{\partial W} & \frac{\partial \dot{Q}}{\partial Q} & \frac{\partial \dot{Q}}{\partial \Theta} \\
 \frac{\partial \dot{\Theta}}{\partial U} & \frac{\partial \dot{\Theta}}{\partial W} & \frac{\partial \dot{\Theta}}{\partial Q} & \frac{\partial \dot{\Theta}}{\partial \Theta}
 \end{bmatrix} \tag{2.32}$$

As can be seen from 2.31 any control law that is to be designed relies heavily on the aerodynamic coefficients of lift, drag and moment. The determination of these values therefore is vital to the accuracy and reliability of the parafoil's performance. The process of theoretical determination and experimental verification of the aerodynamic coefficients of lift and drag is discussed in Chapter 3.

CHAPTER 3. AERODYNAMIC ANALYSIS PROCEDURES

As previously discussed in Chapter 2 there is a need to determine the aerodynamic coefficients of lift and drag in order to implement a design law. In this analysis, three different methods were used to determine the aerodynamic properties of the parafoil: a two dimensional lifting line analysis, a three dimensional modeling program called PMARC, and finally direct experimentation on the parafoil itself using two different angles of incidence.

3.1 Two Dimensional Lifting Line Theory

The common lifting line theory gives accurate results for wings with aspect ratios of five or greater. This derivation of the two dimensional lifting line theory is for low aspect ratio wings. The effect of the air flow over the wing tips has a greater impact on the lift of a wing with a low aspect ratio. Thus, the lift cannot be assumed to be evenly distributed over the surface of the airfoil.

The first step in this analysis is to start with the two-dimensional lift curve slope a_o . This value is stated to be 2π radians⁻¹ from lifting line airfoil theory (Anderson (2)). This value is then applied to a low aspect ratio wing (derived from Lingard (7)).

$$a = \frac{\pi a_o \mathcal{R}}{\pi \mathcal{R} + a_o(1 + \lambda)} \quad (3.1)$$

Equation 3.1 is the lifting slope that takes into account the effect of air flow over the wing tips on the lifting surface. λ is a small positive factor that increases the induced

angle of incidence over that for the minimum case of elliptical loading. For our case, λ is set to 7. Hoerner(4) suggests that for small aspect ratio cases, the lift curve slope, a_o , is reduced by a factor k which is:

$$a'_o = a_o k \quad (3.2)$$

where

$$k = \frac{2\pi \mathcal{R}}{a_o} \tanh \frac{a_o}{2\pi \mathcal{R}} \quad (3.3)$$

Substituting Equations 3.2 and 3.3 into equation 3.1 shows:

$$a = \frac{\pi a'_o \mathcal{R}}{\pi \mathcal{R} + a'_o(1 + \lambda)} \quad (3.4)$$

Equation 3.4 gives the lift slope per radian Lingard ((7)).

Now that there is a lifting line equation that takes into account the changes to the lifting surface, the coefficient of lift can be determined Lingard ((7)).

$$C_L = a(\alpha - \alpha_{ZL}) + K_1 \sin^2(\alpha - \alpha_{ZL}) \cos(\alpha - \alpha_{ZL}) \quad (3.5)$$

Where α_{ZL} is the zero lift angle of attack as determined from the thin airfoil theory and is stated to be zero. K_1 is found from Equation 3.6 as taken from Lingard (7).

$$K_1 = 3.33 - 1.33 \cot \mathcal{R} \quad (3.6)$$

For a wing used as a parafoil the idea of an anhedral is introduced. An anhedral is defined by Figure 3.1.

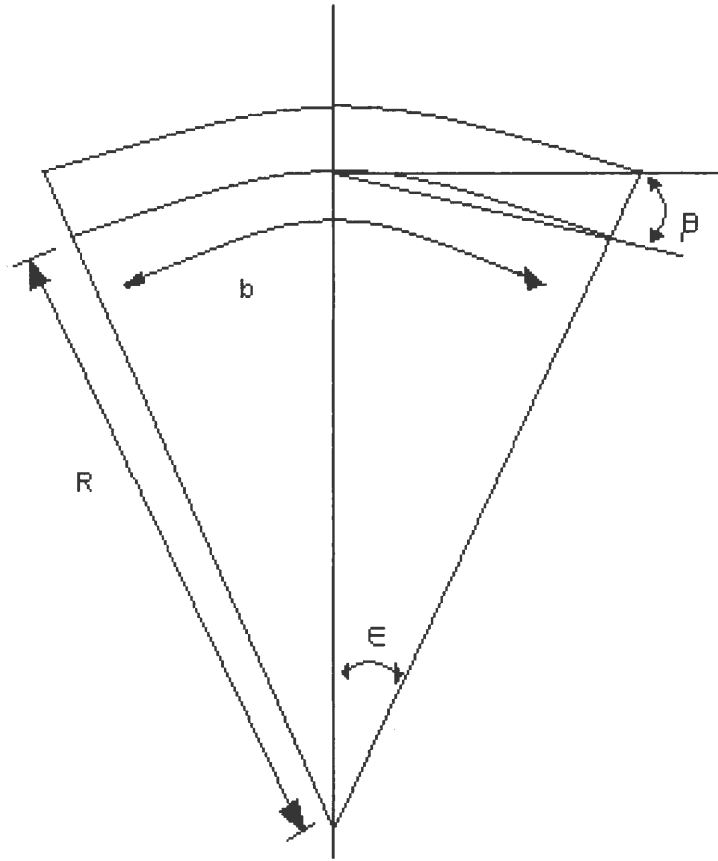


Figure 3.1 Illustration of parafoil geometry including the anhedral angle defined as β

Because the wing is no longer a flat surface the change must be accounted for. It is indicated in Horner (4) that the new C_L can be calculated by:

$$C_L = C_{L\beta=0} \cos^2 \beta \quad (3.7)$$

where β is defined as $\beta = b/4R$ radians where b is the constructed span Lingard ((7)).

Substituting equation 3.7 into 3.5 reveals:

$$C_L = a(\alpha - \alpha_{ZL}) \cos^2 \beta + K_1 \sin^2(\alpha - \alpha_{ZL}) \cos(\alpha - \alpha_{ZL}) \quad (3.8)$$

Drag can be found through its relationship to lift as seen in Equation 3.9 Lingard ((7)).

$$C_D = C_{Do} + \frac{C_L^2(1 + \delta)}{\pi AR} + K_1 \sin^3(\alpha - \alpha_{ZL}) \quad (3.9)$$

Where C_{Do} is the profile drag and δ is a small factor to allow for non-elliptic loading for this analysis. δ in this case is 0.01 (Lingard (7)). As can be seen in equation 3.9 the total drag is made up of two components; the profile drag, C_{Do} , and the induced drag. The profile drag can be broken down to include basic airfoil drag, roughness drag, inlet drag, drag from the strings, and store (payload) drag. Basic airfoil drag and roughness drag are given by Lingard (7) as being 0.015 and 0.004 respectively. Also the procedure for calculating *string drag*, *store drag*, and *inlet drag* is laid out in Lingard (7). *Inlet drag* is calculated by:

$$inlet\ drag = 0.5 \frac{ih}{c} \quad (3.10)$$

where ih is the inlet height and c is the chord length.

The store drag is calculated by:

$$store\ drag = \frac{SP}{S} \quad (3.11)$$

where SP is the area from the store and S is the area of the parafoil

The string drag is calculated by:

$$string\ drag = \frac{nRd(\cos \alpha)^3}{S} \quad (3.12)$$

where n is number of lines, R is the mean line length, d is the line diameter, and α is angle of incidence. For the current parafoil configuration the sum of all of these items is 0.131.

3.2 Panel Method Analysis

After developing a theoretical two dimensional model of the parafoil and getting some values for C_L and C_D , the next step was to develop a three-dimensional model of the parafoil. To do this a program called Panel Method Ames Research Center (PMARC) was used. PMARC is a shareware code developed by NASA. Given a two-dimensional airfoil PMARC can generate a three-dimensional model and then use the vortex panel method to calculate the aerodynamic coefficients. This panel method was chosen over earlier work done by Dr. Tsai because his panel method was a flat sheet (10). The PMARC panel method gives a three dimensional model of the parafoil shape. The closer the two dimensional airfoil shape that is put into PMARC resembles the parafoil the more accurate the PMARC model will be. In an effort to get the two dimensional model to be as close as possible a chord line was drawn on the end of the parafoil. Fifty points were selected on the bottom of the parafoil and fifty points on top, clustering most of the points at the leading edge of the parafoil. The location of each point was measured using the leading edge of the airfoil as the origin and the camber line as the X-axis. These values were then normalized by dividing by the chord length. In order to check the work, the two dimensional airfoil was overlaid onto the parafoil itself as seen in figure 3.2.

The first model of the parafoil had a constant thickness and a constant camber. However after comparing the results from this model to the experimental data the model was unsatisfactory due to the large difference (a factor of five) between the predicted PMARC value and the experimental data. The PMARC model was redesigned to have a thickening of 6 inches, being thickest in the middle and changing to the original thickness at the ends. This change in thickness on the upper surface of the airfoil changes the camber and the aerodynamic coefficients. Once a chord line has been drawn one hundred points on the parafoil were selected.

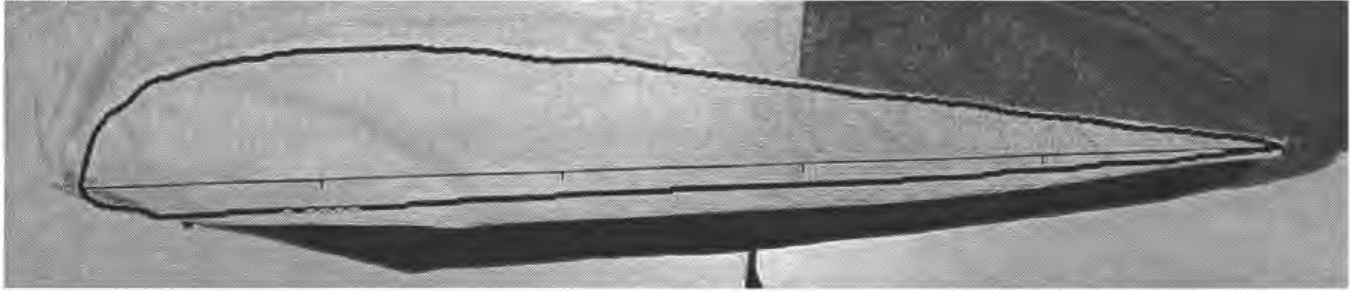


Figure 3.2 Overlay of created airfoil with parafoil

Once the overlay was close, the analysis with PMARC began. Of course there are differences between this three dimensional model and the actual parafoil. Assumptions had to be made to bring the theoretical model in line with an actual model. Some of the assumptions were how much drag was due to the fabric roughness, the drag caused by the inlet at the front of the parafoil in order let air into the parafoil to inflate it, drag caused by pennants on the side of the parafoil, and the drag due to the strings. These effects contribute no lift and only drag. The drag contribution of these effects can be estimated from Lingard (7) and were taken into account when the PMARC results were compared to actual experimental data. The PMARC airfoil for an angle of incidence of three degrees is presented in figure 3.3. The red portions indicate low pressure while the blue indicate high pressure. All of the PMARC airfoils can be seen in appendix A

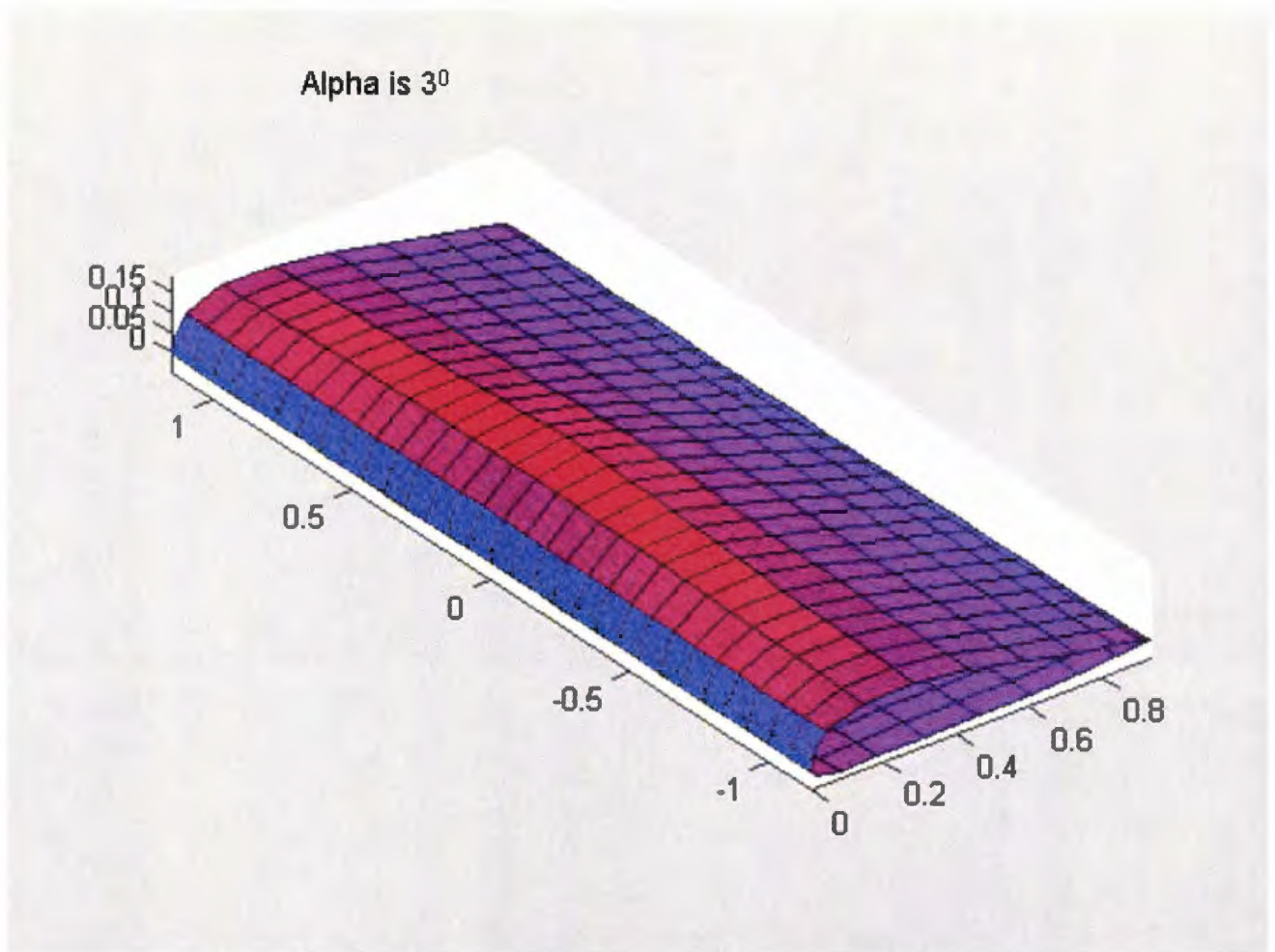


Figure 3.3 PMARC airfoil at angle of incidence of 3 degrees

3.3 Wind Fan Bank

The first experimental attempt at obtaining the lift and drag coefficients of the parafoil was the wind fan bank. The goal behind the wind fan bank was to cut out the expense of balloon drops and to have a much more controlled environment in which to conduct the experiments. The wind fan bank consisted of three industrial sized fans obtained from the Dairy farm at Iowa State University. The fans were all aligned into a wooden frame that could be tilted to various angles. The strings of the parafoil all converged into two lines which were attached to a pair of force transducers. These force

transducers were in turn attached to cement blocks. The set up can be seen in Figure 3.4

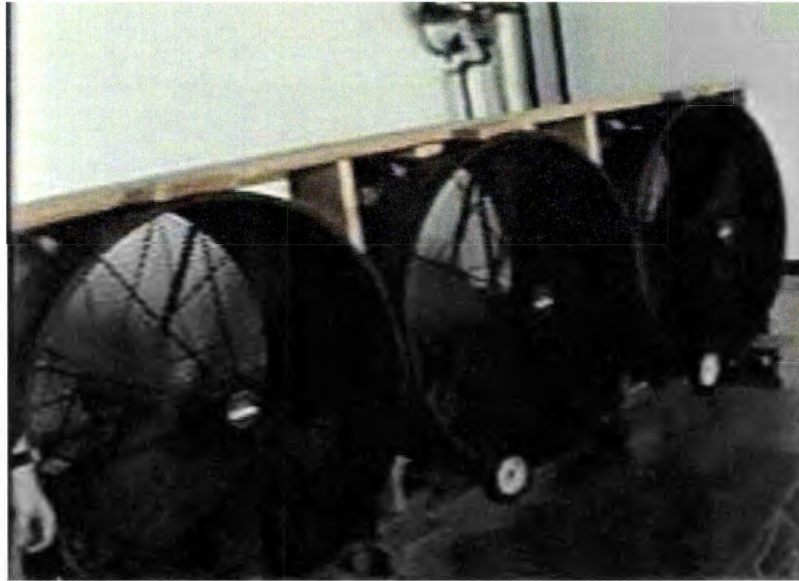


Figure 3.4 Wind fan bank used for lift and drag estimates with the parafoil

By knowing how much force was being exerted on the parafoil and the angle that the string lines made with the cement block, lift and drag could be obtained. Once the wind speed coming out of the fans was measured repeatedly and averaged then the aerodynamic coefficients of lift and drag could be obtained. The failure in this experiment came when the parafoil was inflated by the wind fan bank. The parafoil strings were not set correctly and prevented the parafoil from inflating fully and evenly thus preventing an accurate lift and drag analysis.

3.4 Drop Test Experiment

With the failure of the wind fan bank a new set of experiments had to be devised. Experimental drop tests were the result. The goal of the experimental drop tests was to develop a series of experiments that would reveal the coefficients of lift and drag of the parafoil at several different angles of incidence. This would enable a lift curve line to be drawn and compared to the lift curve line obtained from PMARC and the two-dimensional lifting line. The idea behind this experiment was that the normal condition for the parafoil was that of a glide slope and that the parafoil would naturally want to obtain this position whenever possible.

To start the experiment, a latex balloon is inflated. Attached to the bottom of the balloon is the cut down box and the payload. The balloon is allowed to rise to a given height with two tethers attached to each side of it. Once the balloon is at a height of one hundred to one hundred fifty feet the tether lines are anchored down. A picture of the setup can be seen in Figure 3.5. A laser range finder is then used directly below the balloon/payload to determine the height. The range finder has an accuracy of plus or minus three feet. This measurement is taken directly below the drop box and the location is marked on the ground. The wind and temperature measurements are also taken. The cut down command is then sent to the cut down box. The cut down box contains the electronics which when given the proper command from the command center at the SSOL sends a charge to a nichrome wire. The wire then burns through the cord releasing the payload and parafoil from the cut down box and the balloon. The parafoil is then dropped and ideally deploys into a stable glide slope. Once the parafoil has landed another measurement is taken with the range finder. This time the distance to the parafoil is measured laterally from the same point that the height measurement was taken.

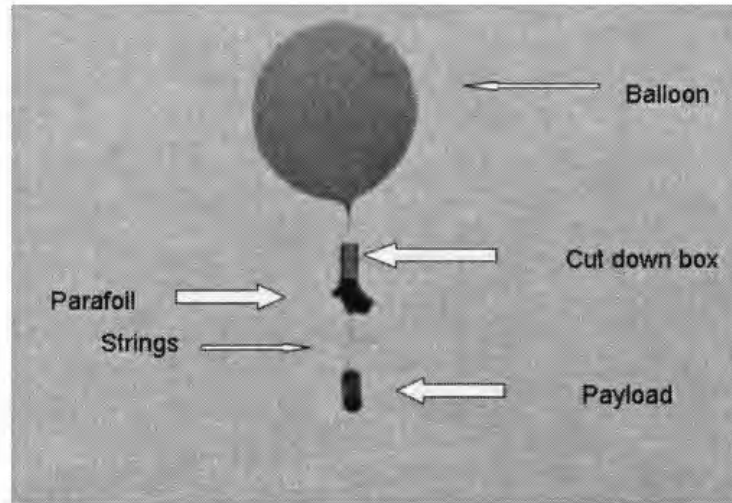


Figure 3.5 Full configuration of balloon experiments

Each drop is recorded using two video cameras each from a different perspective. The data from these cameras were used for several purposes. The first purpose was to determine the deployment height. The parafoil, once released from the cut down box, takes time to deploy. This cuts down on the height at which the glide slope begins, thus biasing the lift and drag calculations. In order to compensate for this, an estimate was made. The height of the parafoil, string lengths, and the payload box are all known quantities. Therefore by reviewing the videotapes of the drop the distance that the parafoil drops can be reasonably estimated. An example of this is shown in Figure 3.6. The second use for the videotape records of each drop was to determine the time it takes the parafoil to land once it has entered the glide slope. Because the distance that the parafoil travels is independently determined, this distance coupled with the time gives the velocity of the parafoil. The velocity was then used in the calculation of the coefficients of lift and drag.

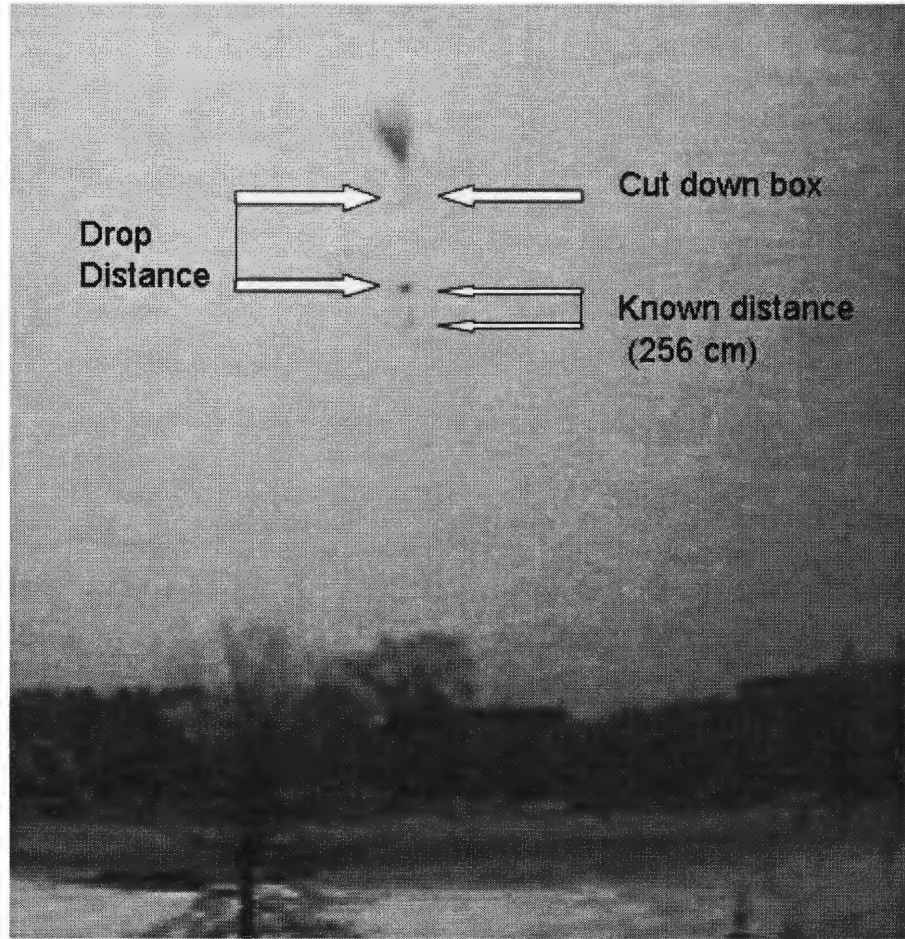


Figure 3.6 A frame from video to illustrate drop distance estimation procedures

The weight of the payload is a predetermined amount. For these tests, the payload was ten pounds of sand. This weight is equivalent to the weight of the electronics for the fully automated guidance system. The payload box, sand, frame and parafoil weighed fifteen pounds. Each configuration of the parafoil was dropped four times to test experiment repeatability.

The angle of incidence of a parafoil is defined as the rigging angle as seen in Figure 3.7.

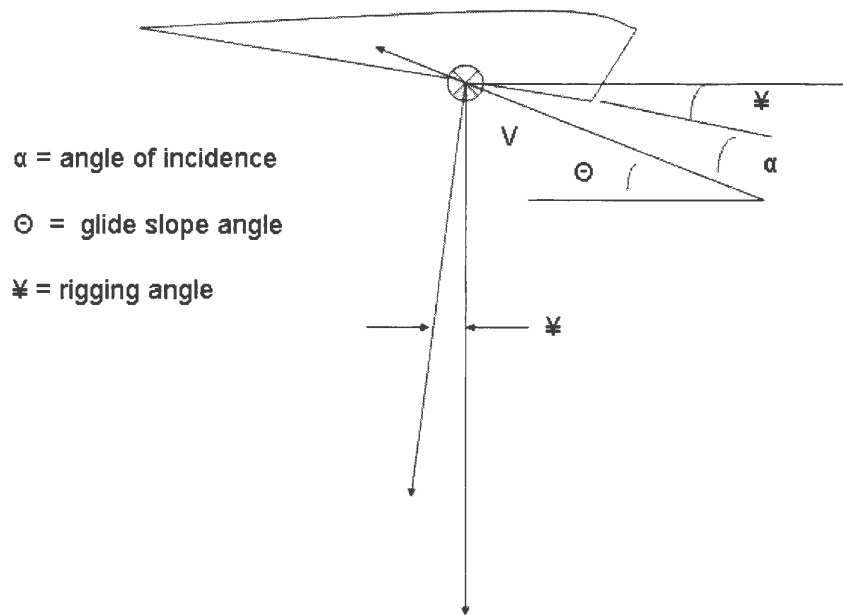


Figure 3.7 Illustration defining glide slope angle and angle of incidence for the parafoil

If the parafoil were gliding horizontal to the ground, then the rigging angle would become the angle of attack that PMARC determined. The two angles of incidence used in this experiment were three degrees and ten degrees. The rigging angle of three degrees was chosen because the data from the lifting line theory at zero angle of incidence shows the C_L to be zero. Three degrees was selected in order to give a positive lift coefficient and to be far enough away from zero degrees for the string lengths to change. A ten degree angle of incidence was used because this was at the top of the lift curve line for a comparable airfoil and yet still provides a comfortable margin of safety from the point of stall of 15 degrees (Lingard (7)).

Once the velocity had been determined and the payload weight was known, the lift and drag of the drop could be calculated. Once the parafoil was in a stable glide slope.

the flight variables shown in Figure 3.8 could be observed and measured.

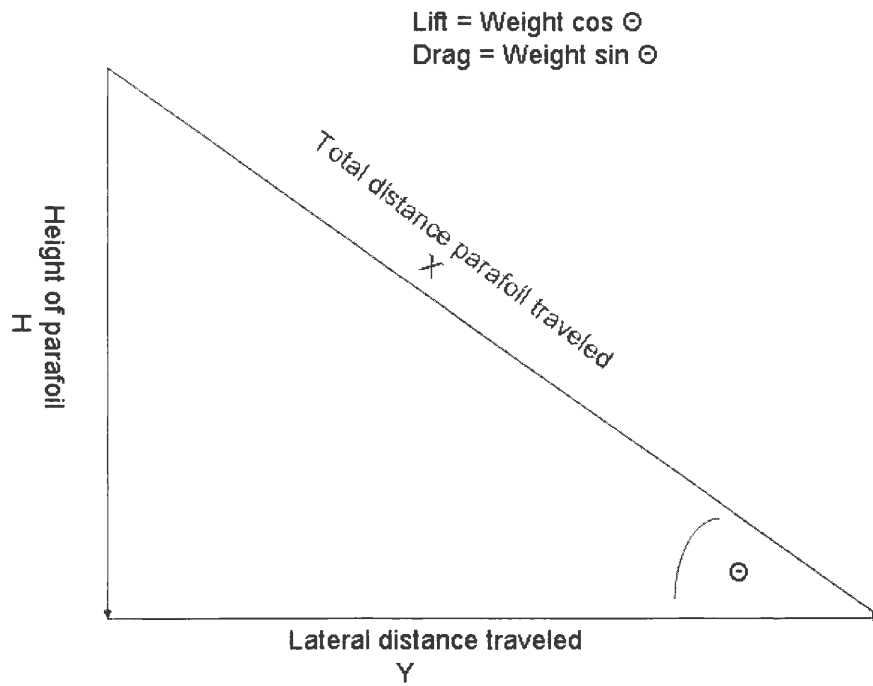


Figure 3.8 Parameters of the glide slope of the parafoil

From these flight variables the lift and drag of the parafoil were computed. From the lift and drag forces the coefficients of lift and drag were calculated. The definitions of the coefficients of lift and drag are shown below in Equations 3.13 and 3.14 respectively.

$$C_L = \frac{L}{q_\infty \cdot S} \quad (3.13)$$

$$C_D = \frac{D}{q_\infty \cdot S} \quad (3.14)$$

$$q_\infty = \frac{\rho}{2} V^2 \quad (3.15)$$

where q_∞ is the dynamic pressure, S is the plan form area of the parafoil, L is lift and D is drag.

The dynamic pressure can be expressed in terms of velocity and air density through equation 3.15 where ρ is the air density and V is velocity. The air density was determined using equation 3.16. The temperature and average pressure for the day were taken from the weather data given by the Ames municipal airport. Once the pressure is known the density can be found from equation 3.16.

$$\rho = \frac{P}{R_g \cdot T} \quad (3.16)$$

where R_g is the air gas constant of $1714 \frac{(ft)(lbs)}{(slug)(R)}$ and ρ is the density.

CHAPTER 4. RECOVERY GUIDANCE SYSTEM EQUIPMENT

This chapter describes the various components that constitute the recover guidance system. In addition to the parafoil, this includes the cut down box for storing the parafoil before deployment, guidance electronics, control lines, and parafoil strings. These are briefly described in this chapter.

4.1 Cut Down Box

The primary purpose of the cut down box is to store the parafoil before deployment. Originally, the parafoil was packed into the box in a lump. As the tests progressed, the sophistication of the packing system also increased. One of the later packing processes for the parafoil entailed packing it in an accordion fashion, then folding the parafoil lengthwise and placing it in the box. In the final configuration, a parachute will be used for heights above twenty five thousand feet.

Once the payload is through the jet stream the parachute will be released and the parafoil will be deployed. In this configuration the parafoil must be as tightly packed as possible. In order to help deployment of the parafoil, a drogue chute system will be used.

A rudimentary release system has been incorporated into the cut down box in order to see if the parafoil will still be reliably deployed after being tightly packed. This release system consists of a Velcro strap glued onto a ring that was sewn into the top of the

parafoil. A string with a rubber band is then tied into the top of the cut down box. When the parafoil is released, the Velcro strap holds the top of the parafoil until the rest of the parafoil has been pulled out of the box by the weight of the payload. This allows the parafoil to spread out quickly and greatly reduces the time it takes to inflate. The rubber band reduces the amount of impulse force on the ring when the parafoil is pulled away from the Velcro strap.

4.2 Differential Global Positioning System

In order for the control law to be implemented and work correctly, the payload must know where it is in relation to the earth. For this purpose the RGS system uses the Global Positioning System (GPS) with differential correction. With ordinary GPS, satellites are used to triangulate the position of the parafoil and where it is in relation to the earth. However, with standard GPS, there is a typical error of ± 300 feet in the vertical direction. Since this is an unacceptable amount of error, a differential GPS (dGPS) receiver is employed to make corrections. By using dGPS the error in the original GPS calculation can be reduced to approximately ± 3 feet. The dGPS receiver uses a known land-based reference location to determine the GPS error. Once this has been calculated, it sends a correction signal to the GPS board, increasing its accuracy. The location information is stored on board once every second and also transmitted to the ground station once every five seconds. The electronics board with the memory module and the GPS boards are assembled and have been tested. The electronic package was not used for the drop test experiments. Due to the fact that currently the RGS is getting a successful deployment of the parafoil about 60 to 70 percent of the time, the payload is a sandbox-the electronics package was deemed too valuable to risk in the experiments. Figures 4.1 and 4.2 show the dGPS board, GPS board, and the memory module respectively.

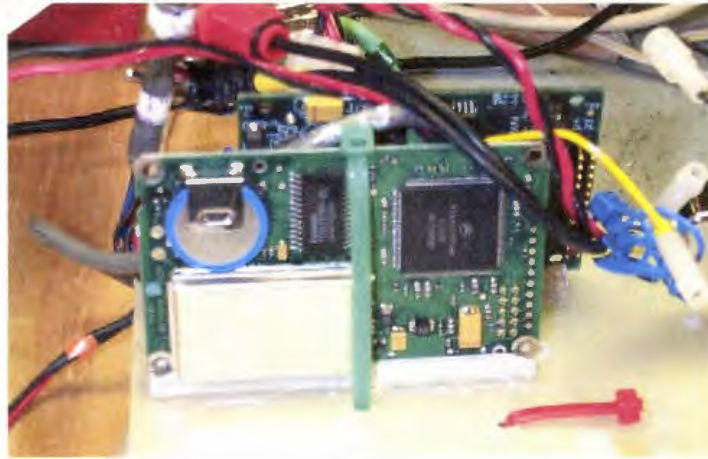


Figure 4.1 Differential Global Positioning board

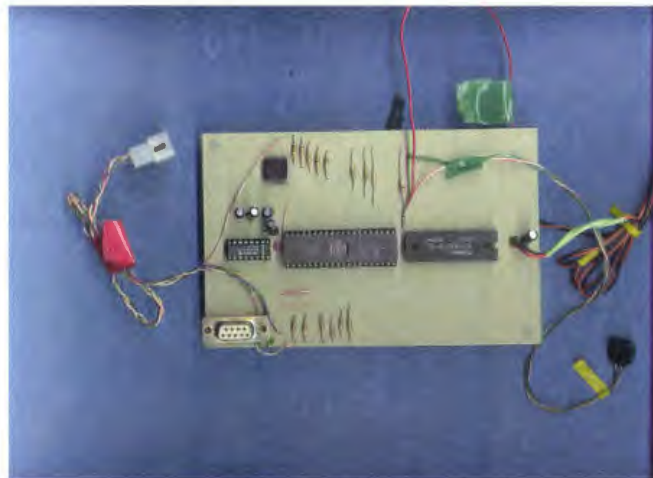


Figure 4.2 Memory Module for data from the DGPS system

4.3 Control Line Servomechanism

The control line servomechanism is a combination of a turning spool, analog to digital converter and analog receiver. The command code is sent out from the command station at 144.3 MHz and received by the analog receiver. The received signal is converted to a digital format and sent to the spool which turns appropriately and pulls on the control

lines of the parafoil. By pulling on the control lines the servomechanism turns the parafoil left or right. The electronic configuration can be seen in Figure 4.3.

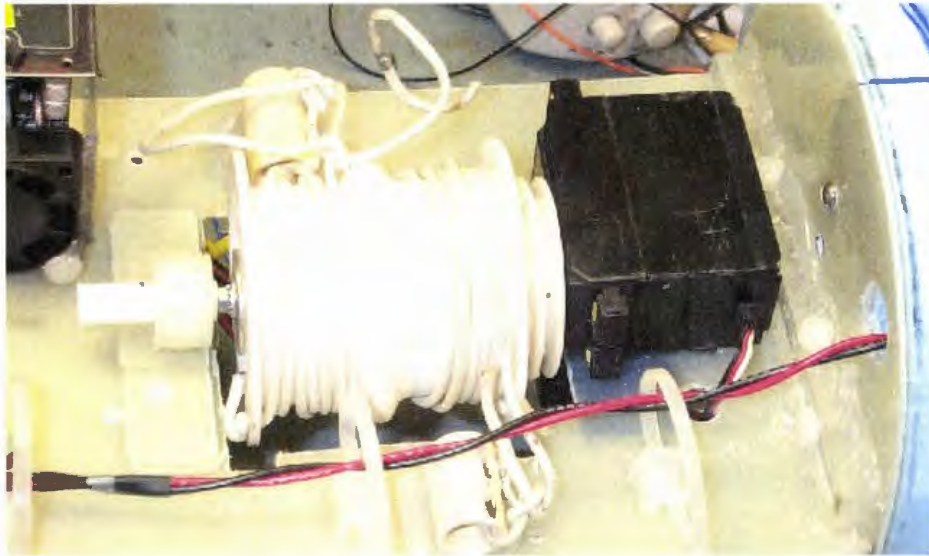


Figure 4.3 Control line servomechanism

4.4 Parafoil Strings

The parafoil is an airfoil with 36 connection points for the strings and 8 for the control lines. Figure 4.4 shows the connection points and control line set up. As can be seen in the figure, the control lines attach to the back of the parafoil creating a control surface. When these strings are pulled the lift of one side of the wing changes creating an uneven moment which turns the parafoil.

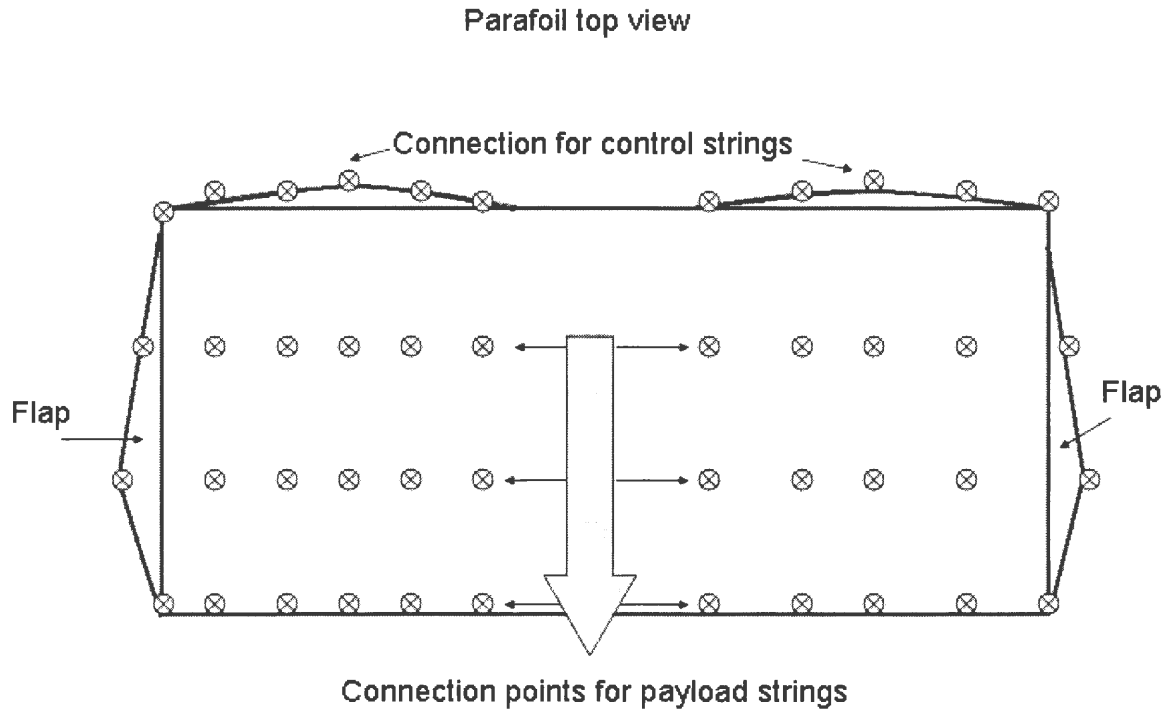


Figure 4.4 Parafoil string configuration

An initial starting design point for string length was $0.6 \cdot b$ where b is the span. This was chosen because this is typical of most parafoils in actual operation (8). Once the lines were set up and the parafoil tested several problems became apparent. When the string lines came together on two rings and the rings were attached to the parafoil, the rings created a pivot point, which rocked the parafoil back and forth. The strings also had a tendency to tangle up during packaging, storage and during flight. In order to fix these problems, a PVC rectangular frame was introduced. The frame had six attachment points on the long sides for the parafoil and four on the corners for the payload. This configuration helped spread out the strings to prevent tangling and also added stability.

CHAPTER 5. RESULTS AND DISCUSSION

This chapter presents the results of each aerodynamic analysis approach. A brief discussion of the comparison between numerical and experimental work then follows.

5.1 Lifting Line Data

The tabulated results for the lifting line theory are listed below. Table 5.1 lists the common constants. Figure 5.1 shows the C_L values of the lifting line analysis with the anhedral angle and without it as the C_L varies with the angle of incidence. Figure 5.2 shows the C_D values of the lifting line analysis with the anhedral angle and without it as the C_D varies with the angle of incidence. This is not the total drag coefficient which would include payload, inlet, strings, etc. Listed below is merely the drag coefficient due to the parafoil. The total drag coefficient is discussed later.

Table 5.1 Common constants in lifting line analysis

a_0	6.28315
a'	5.7577
α	.0493705 degrees
λ	0.07
δ	0.008

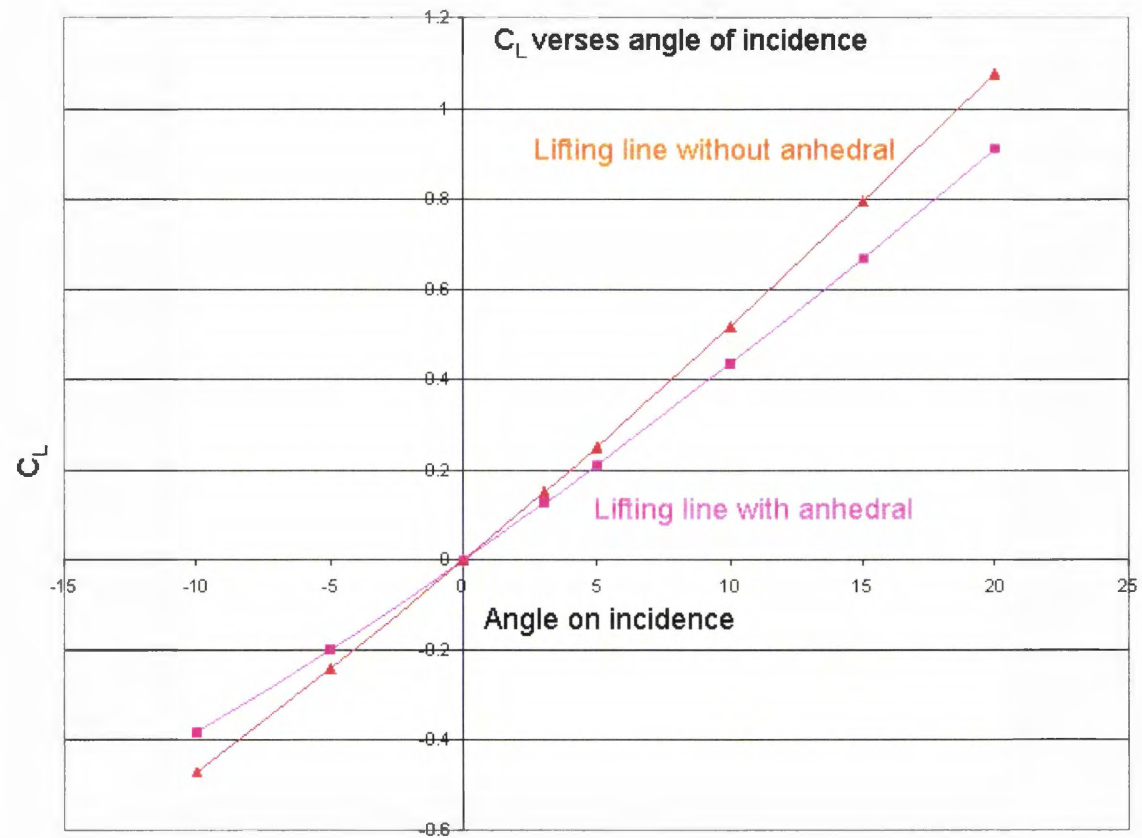


Figure 5.1 Lift coefficient as a function of angle of incidence

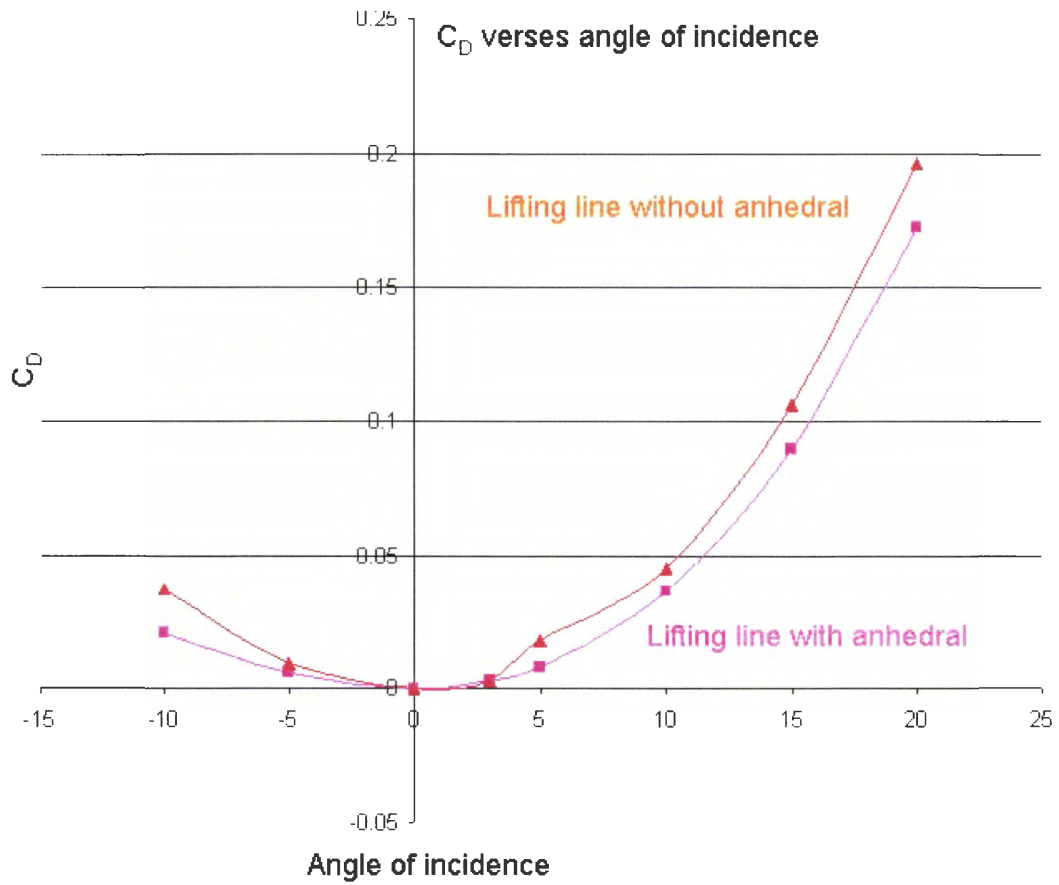


Figure 5.2 Drag coefficient as a function of angle of incidence

5.2 PMARC Results

The two dimensional airfoil geometry used with PMARC is listed in Appendices as well as the PMARC airfoils that were obtained. Shown below in graphs 5.3 and 5.4 are the PMARC results with varying angle of incidence.

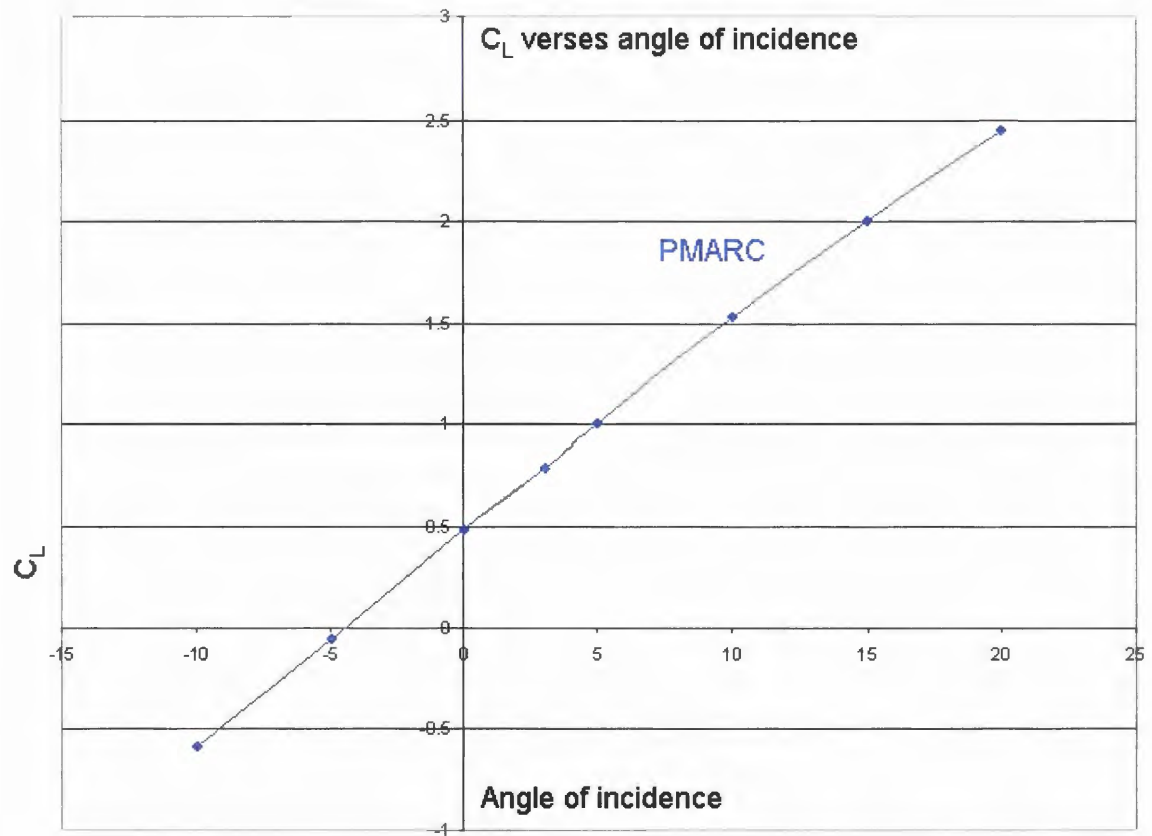


Figure 5.3 Lift coefficient as a function of angle of incidence

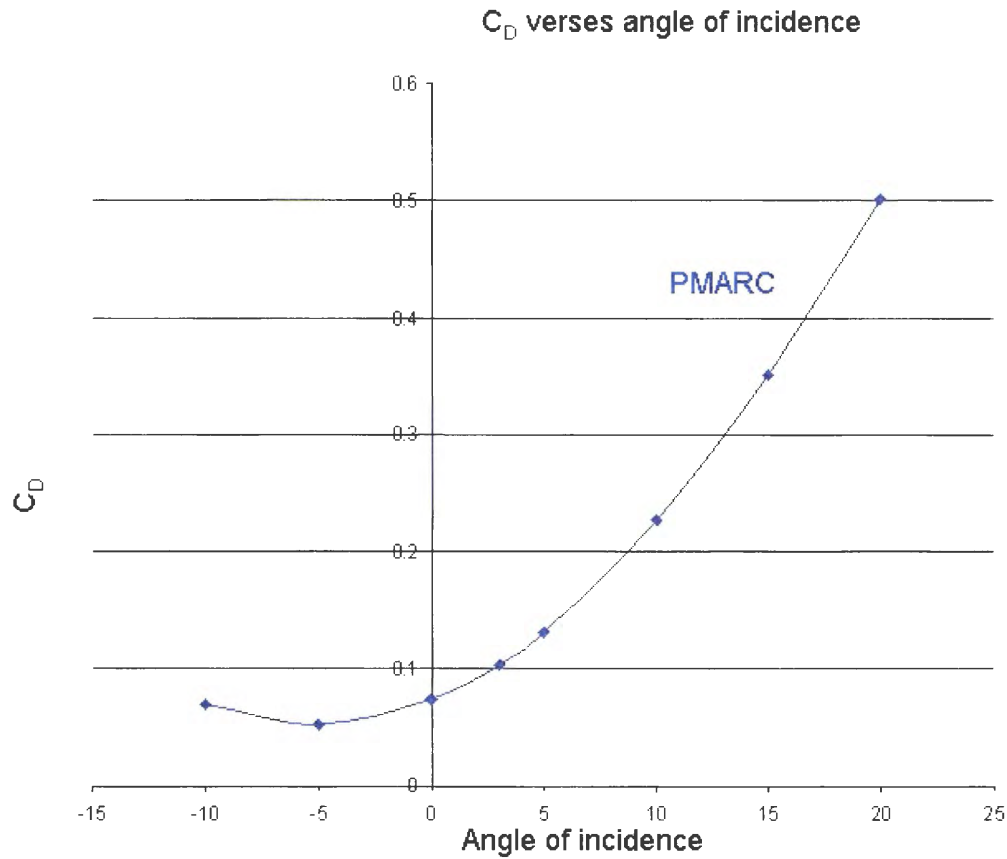


Figure 5.4 Drag coefficient as a function of angle of incidence

5.3 Comparison of PMARC Values to Lifting Line Theory

The next course of action was to compare the results received from the PMARC code to the lifting line theory in order to double check the PMARC values as well as obtain estimates of what should be expected from experimental values. Figure 5.5 shows how the C_L value varies with α for each analytical method. Figure 5.6 shows how the C_D value varies for each method.

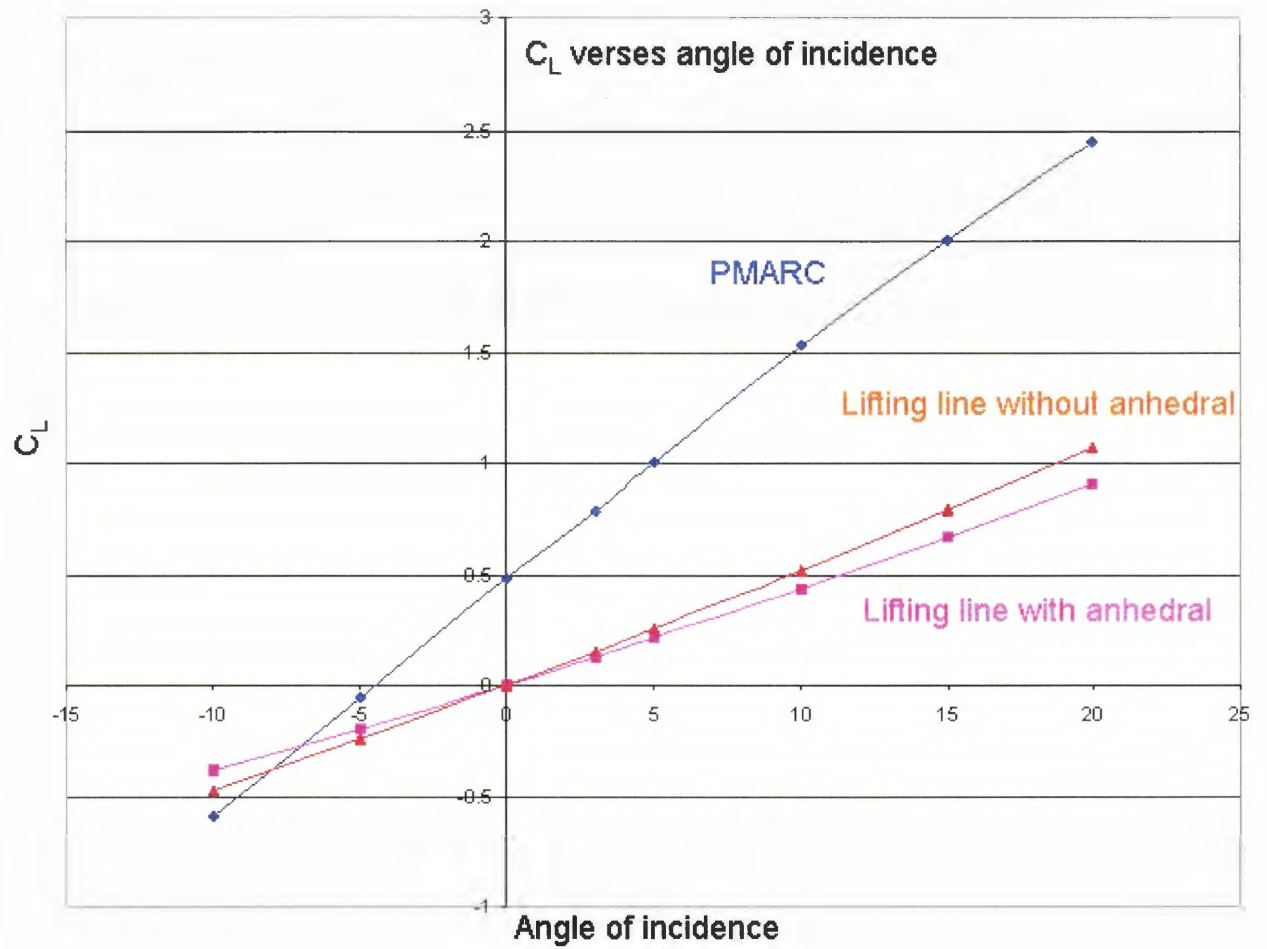


Figure 5.5 Lift coefficient as a function of rigging angle

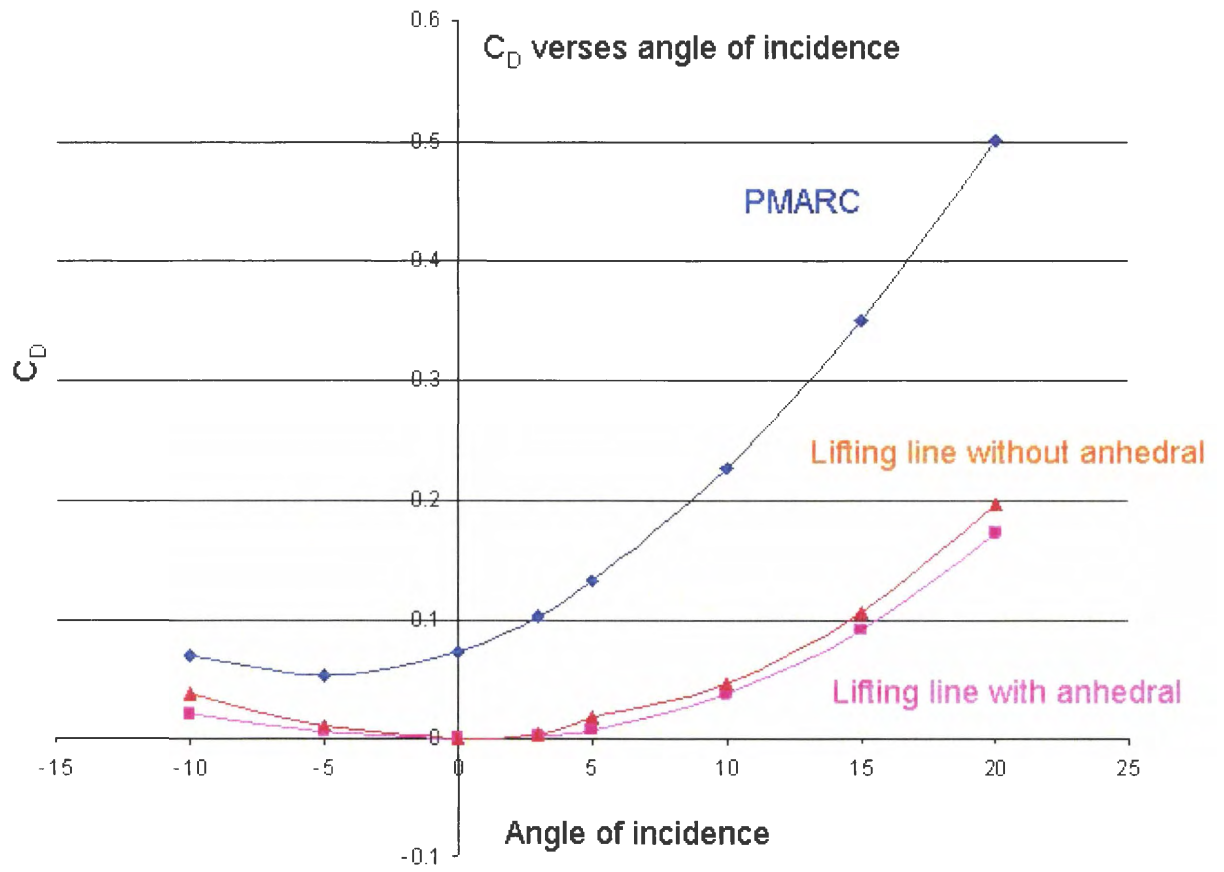


Figure 5.6 Drag coefficient as a function of rigging angle

As can be seen from the graphs, the differences between the two-dimensional lifting line theory and the PMARC values is a small constant. Part of this error stems from the fact that the drag included in the lifting line data is only the induced drag. Also PMARC figuring of induced drag were through surface pressure calculations which may yield inaccurate induced drag coefficients by virtue of course paneling. With this validation, the next step was to acquire experimental values.

5.4 Experimental Results

For the first set of drops the angle of incidence was set at three degrees.

Table 5.2 Results from experimental drops

	Drop number 1	Drop number 2	Drop number 3	Drop number 4
date	1/8/04	1/9/04	1/9/04	1/9/04
measured height	102 ft	135 ft	129 ft	129 ft
lateral distance traveled	75 ft	75 ft	75 ft	90 ft
Parafoil drop distance	28 ft	42 ft	42 ft	34 ft
distance parafoil traveled	105 ft	120 ft	110 ft	131 ft
θ	44.6 degrees	51 degrees	49 degrees	47 degrees
Time traveled	6 seconds	6 seconds	6 seconds	6 seconds
velocity	$18.28 \frac{ft}{s}$	$19.8 \frac{ft}{s}$	$19.14 \frac{ft}{s}$	$21.81 \frac{ft}{s}$
temperature	479.67 R	480.67 R	480.67 R	480.67 R
density	$.0026 \frac{slugs}{ft^3}$	$.0026 \frac{slugs}{ft^3}$	$.0026 \frac{slugs}{ft^3}$	$.0026 \frac{slugs}{ft^3}$
area of parafoil	$29.7 ft^2$	$29.7 ft^2$	$29.7 ft^2$	$29.7 ft^2$
Reynold's number	$5.6 \cdot 10^5$	$6.1 \cdot 10^5$	$5.9 \cdot 10^5$	$6.7 \cdot 10^5$
C_L	0.797	.624	.689	.559
C_D	0.850	.766	.799	.590

The angle of incidence was then set to ten degrees and another set of drops were scheduled. The drops tests occurred on February 15th, 2004. However parafoil did not inflate properly and as a result a glide slope was not obtained. The first drop was from 165 ft and traveled laterally 24 ft. The second drop was again from 165 ft and only traveled laterally 57 ft. The third drop was from 117 ft and traveled laterally 27 ft. The fourth drop was from 141 ft and only traveled 21 ft.

5.5 Comparison of Experimental Data to Theoretical Values

A comparison between the lifting line theory and the PMARC values will be discussed and graphed in the section below. The first table is a comparison between the PMARC values and the experimental results which also includes the mean values for each results and the uncertainty error. The uncertainty error is a combination of the bias error and the precision error. The calculation of this error is discussed in Appendix C.

Table 5.3 Comparison of C_L data of improved PMARC airfoil with experimental data

Drop number	C_L predicted	C_L experiment	percent difference
1	0.7891	.797	1
2	0.7891	.624	21
3	0.7891	.689	13
4	0.7891	.559	30
Mean	0.7891	$.667 \pm 0.240$	16.25

To compare C_D predictions with the experimental results the total drag had to be found. The drag that was calculated in the lifting line theory and PMARC were the parafoil drag. The other drag terms were calculated to be 0.131 as stated in Section 3.1. The parafoil drag coefficient and the drag coefficients from the parafoil, strings, inlet, and payload are added together to get the total drag. This total drag coefficient is then compared to the drag coefficient obtained from the experimental drops in table 5.4.

Table 5.4 Comparison of C_D data of PMARC with experimental data

Drop number	C_D predicted	C_D experiment	percent difference
1	0.2342	0.850	263
2	0.2342	0.766	227
3	0.2342	0.799	241
4	0.2342	0.590	152
Mean	0.2343	0.751 ± 0.265	221

With the addition of the tapering to the PMARC model, the lift coefficient values correspond well. However, the coefficient of drag values still had a large difference between the PMARC calculations and the experimental data. This large difference was very difficult to explain until it was discovered that ram air parafoils like the one that the induced drag values were calculated with have an opening at the rear of parafoil to let air out. On the parafoil for the SSOL there is no opening. This lack of opening would contribute a large drag term. There has been no analysis done to experimentally determine how much drag this lack of an opening would add to the total drag.

CHAPTER 6. CONCLUSIONS AND FUTURE WORK

The angle of incidence of ten degrees was a failure because the experiment did not take into account the fact that the parafoil was much, much smaller than most of the parafoils that have been tested. The research that was done showed that an angle of incidence of ten degrees would be close to the limit of the operable range but still within it. Lingaard (8) stated that the profile drag of the parafoil would be 56 percent of the total drag while the experimentally obtained profile drag was 87.9 percent. The large increase in drag lowered the operational range of the parafoil. Currently tests are underway to find the C_L and C_D at the angles of 6 and -3 degrees to better understand the operational range of the parafoil. The largest source of error in these experiments was the drop estimation. While the procedure that was taken tried to minimize that error, the final estimation was left to the discretion of the observer as to when the parafoil entered the glide slope. A difference of one or two seconds could create a large error in the calculations. Another source of error was the range finder, which has an error of \pm three feet. This error was constant through out the experiment and was part of the accuracy of the equipment used. With all this stated, however, the experimental data still compared favorably with the data obtained from PMARC and the flat plate theory.

This project is currently ongoing. In the last few months work has been done to map out the turning profile of the parafoil. Currently there has been much success in the area. The parafoil now obeys turning inputs from a remote controlled unit. Both left and right turns have been successfully completed. The next stage on the project will be to determine what pulse width modulated signal from the remote control unit gives a

turn of 10 degrees, 40 degrees, and so on.

APPENDIX A. PMARC AIRFOILS

In this appendix are the results from PMARC showing the pressure distribution on the airfoil at various angles of attack.

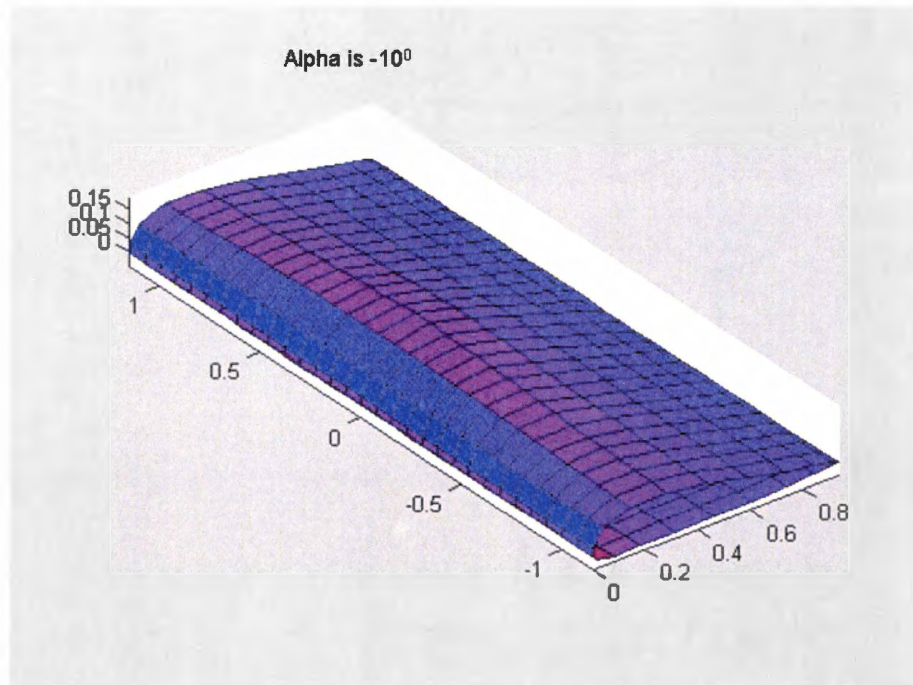


Figure A.1 Pressure distribution results calculated from PMARC for the airfoil at an angle of incidence of -10 degrees

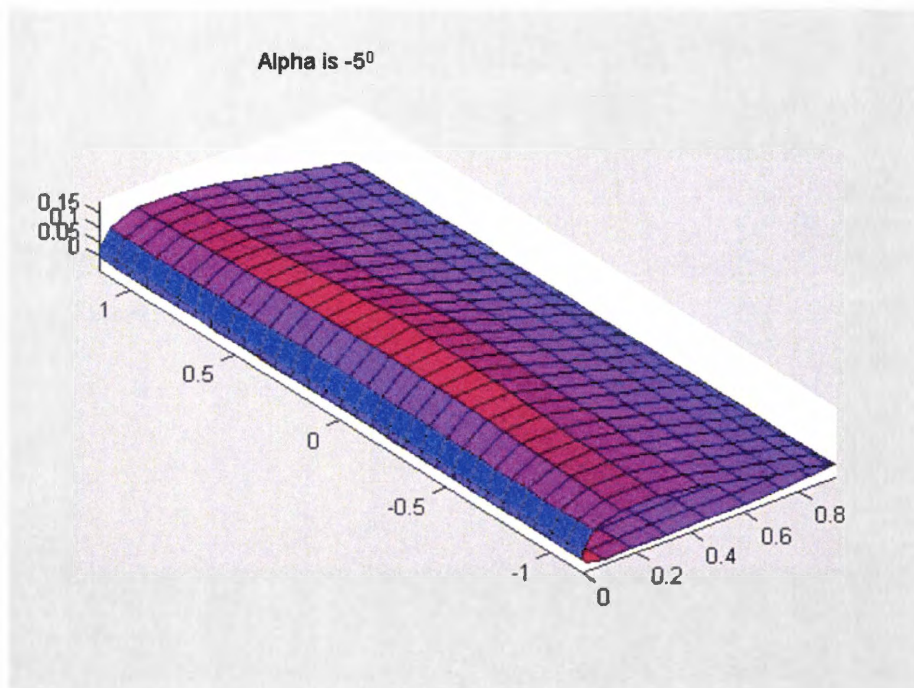


Figure A.2 Pressure distribution results calculated from PMARC for the airfoil at an angle of incidence of -5 degrees

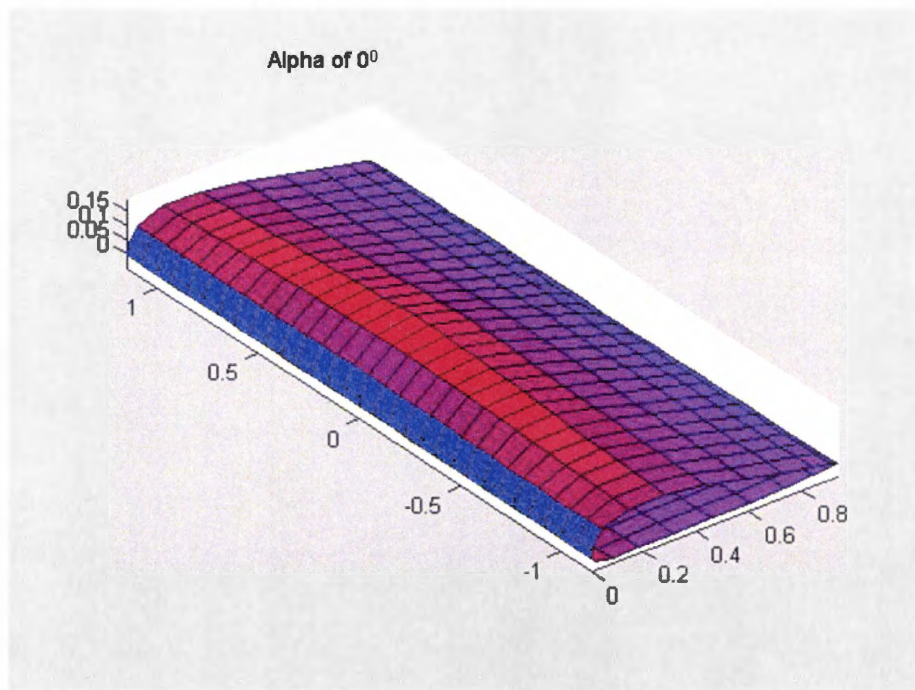


Figure A.3 Pressure distribution results calculated from PMARC for the airfoil at an angle of incidence of zero degrees

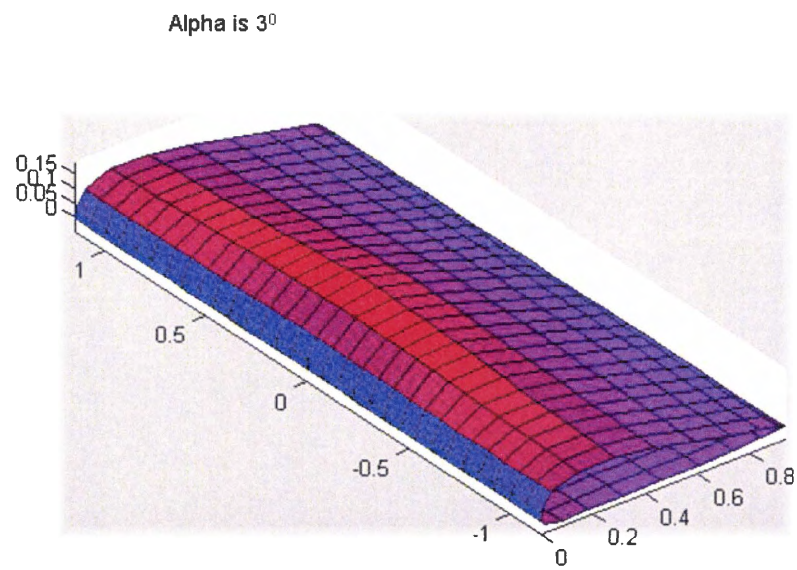


Figure A.4 Pressure distribution results calculated from PMARC for the airfoil at an angle of incidence of 3 degrees

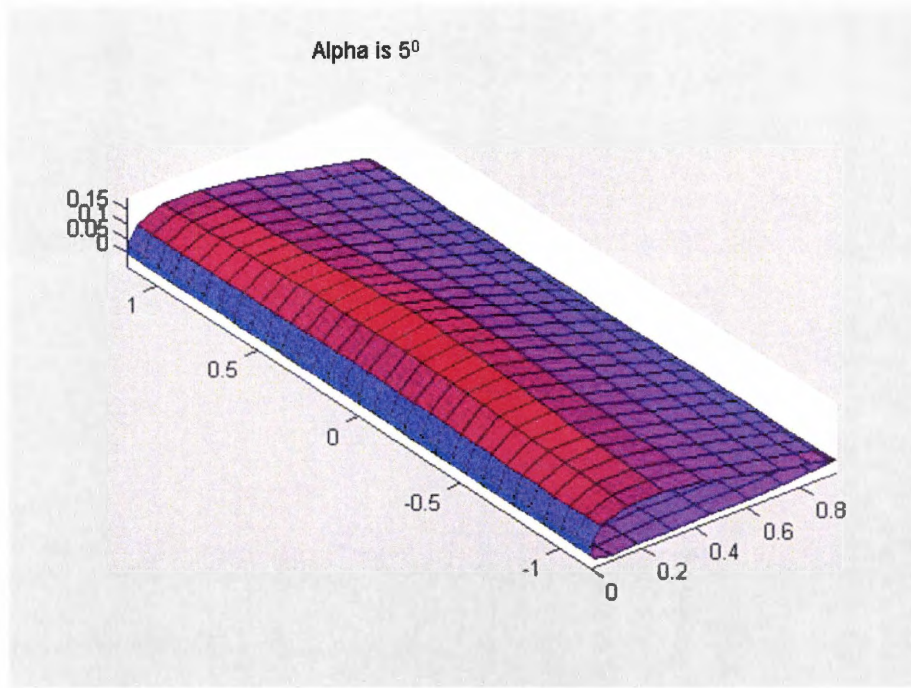


Figure A.5 Pressure distribution results calculated from PMARC for the airfoil at an angle of incidence of 5 degrees

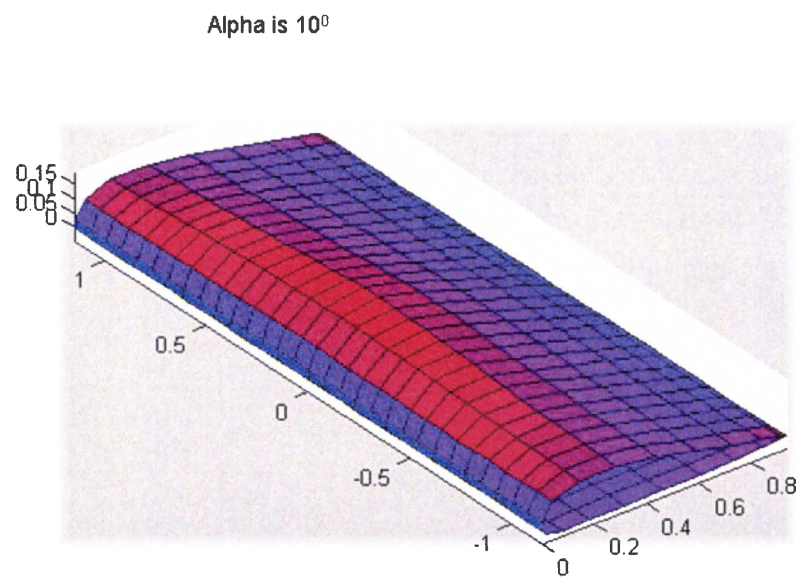


Figure A.6 Pressure distribution results calculated from PMARC for the airfoil at an angle of incidence of 10 degrees

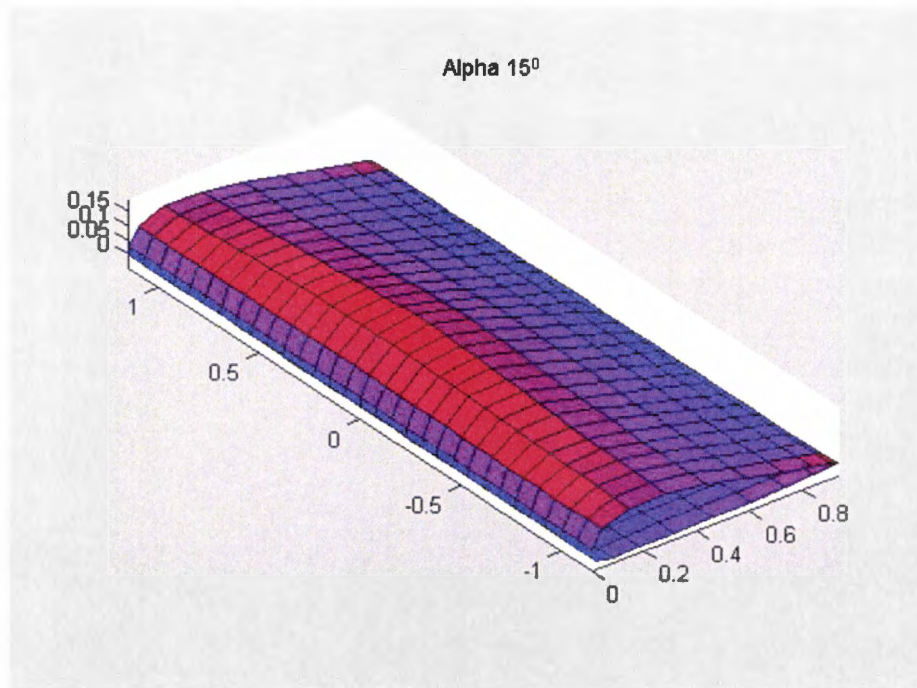


Figure A.7 Pressure distribution results calculated from PMARC for the airfoil at an angle of incidence of 15 degrees

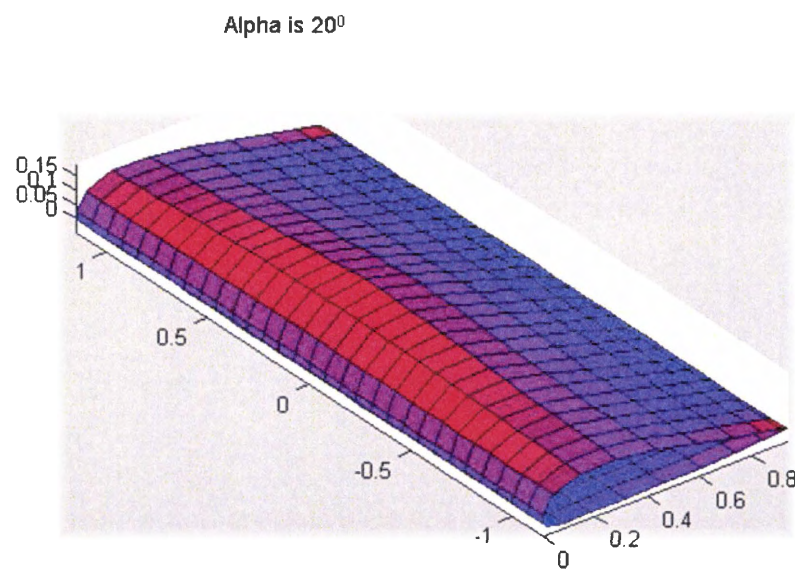


Figure A.8 Pressure distribution results calculated from PMARC for the airfoil at an angle of incidence of 20 degrees

APPENDIX B. AIRFOIL INPUT GEOMETRY FOR PMARC

Table B.1 The PMARC panels input without tapering

Upper surface		Lower surface	
0	0.000	0.0000	0.0000
0.011	0.027	0.0081	-0.0134
0.022	0.048	0.0215	-0.0188
0.032	0.059	0.0323	-0.0247
0.043	0.070	0.0430	-0.0280
0.054	0.077	0.0538	-0.0323
0.065	0.091	0.0645	-0.0384
0.075	0.094	0.0753	-0.0384
0.086	0.099	0.0860	-0.0384
0.097	0.102	0.0968	-0.0384
0.108	0.104	0.1075	-0.0384
0.118	0.108	0.1183	-0.0384
0.129	0.108	0.1290	-0.0363
0.14	0.108	0.1398	-0.0363
0.151	0.109	0.1505	-0.0363
0.161	0.111	0.1613	-0.0363
0.172	0.111	0.1720	-0.0363
0.183	0.111	0.1828	-0.0363
0.194	0.112	0.1935	-0.0363
0.204	0.112	0.2043	-0.0363
0.215	0.112	0.2151	-0.0363
0.226	0.112	0.2258	-0.0363
0.237	0.113	0.2366	-0.0363
0.247	0.113	0.2473	-0.0363
0.258	0.112	0.2581	-0.0363
0.269	0.110	0.2688	-0.0323
0.28	0.109	0.2796	-0.0296
0.29	0.108	0.2903	-0.0269
0.301	0.106	0.3011	-0.0258
0.312	0.104	0.3118	-0.0258
0.323	0.103	0.3226	-0.0247
0.355	0.099	0.3548	-0.0247
0.387	0.094	0.3871	-0.0237
0.452	0.081	0.4194	-0.0226
0.484	0.072	0.4516	-0.0226
0.516	0.067	0.4839	-0.0215
0.548	0.061	0.5161	-0.0204
0.581	0.056	0.5484	-0.0204
0.613	0.052	0.6129	-0.0204
0.645	0.047	0.6452	-0.0204
0.677	0.041	0.6774	-0.0194
0.71	0.035	0.7097	-0.0183
0.774	0.027	0.7419	-0.0172
0.806	0.022	0.7742	-0.0161
0.839	0.017	0.8065	-0.0151
0.871	0.013	0.8710	-0.0118
0.903	0.010	0.9032	-0.0108
0.935	0.006	0.9355	-0.0065
0.968	0.003	0.9677	-0.0043
1	0.000	1.0000	0.0000

Table B.2 The PMARC panels input with tapering for upper surface

Upper surface							
Panel 1		Panel 2		Panel 3		Panel 4	
0	0	0	0	0	0	0	0
0.0108	0.0484	0.0108	0.0484	0.0108	0.0484	0.0108	0.0484
0.0215	0.0699	0.0215	0.0699	0.0215	0.0699	0.0215	0.0699
0.0323	0.0946	0.0323	0.0946	0.0323	0.0946	0.0323	0.0806
0.043	0.1089	0.043	0.1089	0.043	0.1089	0.043	0.0887
0.0538	0.1247	0.0538	0.1175	0.0538	0.1175	0.0538	0.1022
0.0645	0.1312	0.0645	0.1261	0.0645	0.1261	0.0645	0.1086
0.0753	0.1398	0.0753	0.1348	0.0753	0.1312	0.0753	0.1118
0.086	0.1495	0.086	0.1419	0.086	0.1366	0.086	0.1151
0.0968	0.1559	0.0968	0.1505	0.0968	0.1419	0.0968	0.1204
0.1075	0.1645	0.1075	0.1591	0.1075	0.1452	0.1075	0.1226
0.1183	0.1706	0.1183	0.1699	0.1183	0.1505	0.1183	0.1247
0.129	0.1782	0.129	0.1753	0.129	0.1505	0.129	0.1269
0.1398	0.1839	0.1398	0.1785	0.1398	0.1538	0.1398	0.128
0.1538	0.1946	0.1505	0.1785	0.1505	0.1538	0.1505	0.129
0.1613	0.1959	0.1613	0.1806	0.1613	0.1559	0.1613	0.1312
0.172	0.2	0.172	0.1828	0.172	0.1581	0.172	0.1333
0.1828	0.2033	0.1828	0.1839	0.1828	0.1591	0.1828	0.1344
0.1935	0.2068	0.1935	0.1839	0.1935	0.1591	0.1935	0.1344
0.2043	0.2086	0.2043	0.1839	0.2043	0.1591	0.2043	0.1344
0.2258	0.2086	0.2258	0.1839	0.2258	0.1591	0.2258	0.1344
0.2366	0.2086	0.2366	0.1839	0.2366	0.1591	0.2366	0.1344
0.2473	0.2097	0.2473	0.1849	0.2473	0.1602	0.2473	0.1355
0.2581	0.2097	0.2581	0.1849	0.2581	0.1602	0.2581	0.1355
0.2688	0.2086	0.2688	0.1839	0.2688	0.1591	0.2688	0.1344
0.2796	0.2086	0.2796	0.1839	0.2796	0.1591	0.2796	0.1344
0.2903	0.2065	0.2903	0.1817	0.2903	0.157	0.2903	0.1323
0.3011	0.2054	0.3011	0.1806	0.3011	0.1559	0.3011	0.1312
0.3118	0.2054	0.3118	0.1806	0.3118	0.1559	0.3118	0.1312
0.3226	0.202	0.3226	0.1806	0.3226	0.1559	0.3226	0.1312
0.3548	0.1956	0.3548	0.172	0.3548	0.1485	0.3548	0.1247
0.3871	0.1858	0.3871	0.1634	0.3871	0.1411	0.3871	0.1183
0.4194	0.176	0.4194	0.1548	0.4194	0.1336	0.4194	0.1151
0.4516	0.1663	0.4516	0.1462	0.4516	0.1262	0.4516	0.1129
0.4839	0.1565	0.4839	0.1376	0.4839	0.1188	0.4839	0.1043
0.5161	0.1467	0.5161	0.129	0.5161	0.1114	0.5161	0.0968
0.5484	0.1369	0.5484	0.1204	0.5484	0.1039	0.5484	0.0914
0.5806	0.1271	0.5806	0.1118	0.5806	0.0965	0.5806	0.0839
0.6129	0.1174	0.6129	0.1032	0.6129	0.0891	0.6129	0.0774
0.6452	0.1076	0.6452	0.0946	0.6452	0.0817	0.6452	0.0699
0.6774	0.0978	0.6774	0.0867	0.6774	0.0742	0.6774	0.0645
0.7419	0.0782	0.7419	0.0688	0.7419	0.0594	0.7419	0.0538
0.7742	0.0685	0.7742	0.0602	0.7742	0.052	0.7742	0.0462
0.8065	0.0587	0.8065	0.0516	0.8065	0.0445	0.8065	0.0387
0.8387	0.0489	0.8387	0.043	0.8387	0.0371	0.8387	0.0344
0.871	0.0391	0.871	0.0344	0.871	0.0297	0.871	0.0269
0.9032	0.0293	0.9032	0.0258	0.9032	0.0223	0.9032	0.0215
0.9355	0.0196	0.9355	0.0172	0.9355	0.0148	0.9355	0.0161
0.9677	0.0098	0.9677	0.0086	0.9677	0.0074	0.9677	0.0108
1	0	1	0	1	0	1	0

Table B.3 The PMARC panels input with tapering for lower surface

Lower Surface							
Panel 1		Panel 2		Panel 3		Panel 4	
0	0	0	0	0	0	0	0
0.0081	-0.0134	0.0081	-0.0134	0.0081	-0.0134	0.0081	-0.0134
0.0215	-0.0215	0.0215	-0.0215	0.0215	-0.0188	0.0215	-0.0188
0.0323	-0.0296	0.0323	-0.0269	0.0323	-0.0247	0.0323	-0.0215
0.043	-0.0376	0.043	-0.0344	0.043	-0.028	0.043	-0.0242
0.0538	-0.0457	0.0538	-0.0409	0.0538	-0.0323	0.0538	-0.0269
0.0645	-0.0508	0.0645	-0.0446	0.0645	-0.0384	0.0645	-0.0323
0.0753	-0.0508	0.0753	-0.0446	0.0753	-0.0384	0.0753	-0.0323
0.086	-0.0508	0.086	-0.0446	0.086	-0.0384	0.086	-0.0323
0.0968	-0.0508	0.0968	-0.0446	0.0968	-0.0384	0.0968	-0.0323
0.1075	-0.0508	0.1075	-0.0446	0.1075	-0.0384	0.1075	-0.0323
0.1183	-0.0508	0.1183	-0.0446	0.1183	-0.0384	0.1183	-0.0323
0.129	-0.0487	0.129	-0.0425	0.129	-0.0363	0.129	-0.0301
0.1398	-0.0487	0.1398	-0.0425	0.1398	-0.0363	0.1398	-0.0301
0.1505	-0.0487	0.1505	-0.0425	0.1505	-0.0363	0.1505	-0.0301
0.1613	-0.0487	0.1613	-0.0425	0.1613	-0.0363	0.1613	-0.0301
0.172	-0.0487	0.172	-0.0425	0.172	-0.0363	0.172	-0.0301
0.1828	-0.0487	0.1828	-0.0425	0.1828	-0.0363	0.1828	-0.0301
0.1935	-0.0487	0.1935	-0.0425	0.1935	-0.0363	0.1935	-0.0301
0.2043	-0.0487	0.2043	-0.0425	0.2043	-0.0363	0.2043	-0.0301
0.2151	-0.0487	0.2151	-0.0425	0.2151	-0.0363	0.2151	-0.0301
0.2258	-0.0487	0.2258	-0.0425	0.2258	-0.0363	0.2258	-0.0301
0.2366	-0.0487	0.2366	-0.0425	0.2366	-0.0363	0.2366	-0.0301
0.2473	-0.0487	0.2473	-0.0425	0.2473	-0.0363	0.2473	-0.0301
0.2581	-0.0487	0.2581	-0.0425	0.2581	-0.0363	0.2581	-0.0301
0.2688	-0.0475	0.2688	-0.0384	0.2688	-0.0323	0.2688	-0.0301
0.2796	-0.0441	0.2796	-0.0358	0.2796	-0.0296	0.2796	-0.028
0.2903	-0.0414	0.2903	-0.0331	0.2903	-0.0269	0.2903	-0.028
0.3011	-0.0394	0.3011	-0.032	0.3011	-0.0258	0.3011	-0.028
0.3118	-0.0382	0.3118	-0.032	0.3118	-0.0258	0.3118	-0.028
0.3226	-0.0371	0.3226	-0.0309	0.3226	-0.0247	0.3226	-0.0269
0.3548	-0.0353	0.3548	-0.0294	0.3548	-0.0247	0.3548	-0.0269
0.3871	-0.0336	0.3871	-0.028	0.3871	-0.0237	0.3871	-0.0258
0.4194	-0.0318	0.4194	-0.0265	0.4194	-0.0226	0.4194	-0.0247
0.4516	-0.03	0.4516	-0.025	0.4516	-0.0226	0.4516	-0.0247
0.4839	-0.0283	0.4839	-0.0236	0.4839	-0.0215	0.4839	-0.0237
0.5161	-0.0265	0.5161	-0.0221	0.5161	-0.0204	0.5161	-0.0226
0.5484	-0.0247	0.5484	-0.0206	0.5484	-0.0204	0.5484	-0.0226
0.6129	-0.0212	0.6129	-0.0177	0.6129	-0.0204	0.6129	-0.0226
0.6452	-0.0194	0.6452	-0.0162	0.6452	-0.0204	0.6452	-0.0226
0.6774	-0.0177	0.6774	-0.0147	0.6774	-0.0194	0.6774	-0.0215
0.7097	-0.0159	0.7097	-0.0132	0.7097	-0.0183	0.7097	-0.0204
0.7419	-0.0141	0.7419	-0.0118	0.7419	-0.0172	0.7419	-0.0194
0.7742	-0.0124	0.7742	-0.0103	0.7742	-0.0161	0.7742	-0.0161
0.8065	-0.0106	0.8065	-0.0088	0.8065	-0.0151	0.8065	-0.0151
0.871	-0.0071	0.871	-0.0059	0.871	-0.0118	0.871	-0.0118
0.9032	-0.0053	0.9032	-0.0044	0.9032	-0.0108	0.9032	-0.0108
0.9355	-0.0035	0.9355	-0.0029	0.9355	-0.0065	0.9355	-0.0065
0.9677	-0.0018	0.9677	-0.0015	0.9677	-0.0043	0.9677	-0.0043
1	0	1	0	1	0	1	0

APPENDIX C. UNCERTAINTY ANALYSIS

Any discussion of the data from an experiment must include the uncertainty of that data. The approach followed is outlined in Beckwith and Marangoni (9). The uncertainty analysis consists of two parts the bias error and the precision error. The bias error is the error inherent in the equipment used and the precision of the measurements. Once this error has been defined it is constant throughout the experiment. The precision error is the randomness of the variables. Meaning that if you perform the experiment N number of times you will not always get the same result.

C.1 Precision Error

The first aspect of the uncertainty analysis is that of precision error. The precision error is the range of which the true value of the unknown value should value. The method of finding the precision error is outlined in Figliola and Beasley (11). The first step in this procedure is to find the mean value of the data set. For this analysis the data set consists of four drops. This procedure is shown in equation C.1.

$$\bar{x} = \frac{1}{4} \sum x_i \tag{C.1}$$

where \bar{x} is the mean value. The next step in the process is to compute the sample standard standard deviation.

$$S_x = \sqrt{\frac{1}{3} \sum x_i(x_i - \bar{x})} \quad (\text{C.2})$$

where S_x is the standard deviation. The final step is to find the precision interval. This can be done with equation C.3.

$$S_x = \frac{S_x \cdot t_{v,95}}{4} \quad (\text{C.3})$$

where $t_{v,95}$ is the student t distribution. For this analysis the student t distribution is 3.182 Beasley (11). The final precision index for this analysis on the C_L is ± 0.161 at 95 percent and the precision index for the C_D is ± 0.180 at 95 percent.

C.2 Bias Error

The first step in the bias error analysis is to define the equations used in terms of the measured variables.

$$Lift = wt \cdot \frac{x}{\sqrt{H^2 + x^2}} \quad (\text{C.4})$$

$$Drag = wt \cdot \frac{H}{\sqrt{H^2 + x^2}} \quad (\text{C.5})$$

$$C_L = \frac{Lift}{\frac{1}{2} \cdot \rho V^2} \quad (\text{C.6})$$

$$C_D = \frac{Drag}{\frac{1}{2} \cdot \rho V^2} \quad (\text{C.7})$$

$$Velocity = \frac{\sqrt{x^2 + H^2}}{t} \quad (\text{C.8})$$

The next step is to determine the uncertainty of the variables in the basic equations. Once that has been found the uncertainty of the lift, drag, and their corresponding coefficients can be determined.

Equation C.4 lift is made up of three variables, parafoil height (h), the distance the parafoil traveled laterally (x), and the weight wt of the parafoil system (payload, parafoil, strings, etc.). Now the uncertainty of each one of these variable will be determined beginning with the parafoil height (h). Uncertainty in the height measurement from the range finder was \pm three feet (Uh_1), while the estimation of how far the parafoil fell before it maintained a steady glide slope was estimated to be \pm four feet (Uh_2). Following equation C.9, uncertainty for the height of the parafoil(Uh) was \pm five feet.

$$Uh = \sqrt{(Uh_1)^2 + (Uh_2)^2} \quad (C.9)$$

The next step is to find the uncertainty of the distance the parafoil traveled laterally (Ux). The uncertainty of the lateral distance was made up of two parts. The first part was from the range finder this uncertainty was \pm three feet. The second part of the uncertainty in the lateral distance was from the drift of the balloon, meaning how far the balloon drifted in the lateral plane after the height measurement was taken and the position marked on the ground. This distance was estimated at \pm six feet. Giving an uncertainty for Ux of \pm 6.7 feet.

The last variable to determine the uncertainty of lift is the weight (Uwt). Uncertainty in this variable came from the accuracy of the scale. This uncertainty was estimated to be \pm .25 lbs_f. An uncertainty also came from the sand that may have leaked out during a hard impact with the ground. Even though the leakage was considered minimal it was estimated at .1 lbs_f. This leads to a total uncertainty of .353lbs_f for the Uwt term. Now that the uncertainty of all the terms that make up the lift have been quantified, the uncertainty of the lift (Ul) itself can be found. This is done using equation C.10

$$Ul = \sqrt{(Ux \cdot \frac{\partial Lift}{\partial x})^2 + (Uh \cdot \frac{\partial Lift}{\partial h})^2 + (Uwt \cdot \frac{\partial Lift}{\partial wt})^2} \quad (C.10)$$

The next step is to determine the uncertainty of the drag. As can be seen from equation C.7 the drag uncertainty is made up of the same terms as lift uncertainty, only varying by the partial derivatives.

Now that we have determined the uncertainty of the lift and drag variables, the uncertainty of the aerodynamic coefficients can be determined. As stated in equations 3.13 and 3.14, the coefficients of lift and drag are each made up of four variables: the span of the parafoil (s), the velocity of the parafoil (v), the density of the air (ρ), and the variables of lift and drag respectively. Before the uncertainty of the other variables can be determined it must first be noted that the variable of velocity is itself made up of several variables as can be seen in equation C.11.

$$v = \frac{\sqrt{x^2 + h^2}}{t} \quad (C.11)$$

The uncertainty of x and h have already been established. All that is left is to determine the uncertainty of time (t). The timing device used for the experiment moved in increments of one second and so the uncertainty of the time measurement was ± 0.5 seconds. The total uncertainty of the velocity can be found using the same method as shown in equation C.10.

The next step in determining the uncertainty of the coefficients is to determine the uncertainty in ρ ($u\rho$). ρ is made up of two variables, temperature (T) and pressure (P). The value for the temperature measurement was taken the national weather site at the Ames municipal airport. The uncertainty of the temperature is the error in the airport instruments, which in this case was estimated to be one degree Rankine. The difference between the launch site and the airport was estimated to be 4 Rankine, and the variation of the temperature during the experiment which was estimated at 10

Rankine. The uncertainty for the pressure measurement was similar. The uncertainty in the airport's equipment was estimated to be 0.01 in Hg, the difference between the launch site and the airport was estimated at 0.1 in Hg, and the variation of the pressure throughout the day was estimated at .5 in Hg. From these two uncertainty measurements the uncertainty of ρ can now be obtained.

Once the uncertainty of ρ has been determined there is only more uncertainty variable needs to be determined, that of the area of the parafoil (s). This value was measured to be 29.7 ft². The uncertainty of this was $\frac{1}{8}$ inch in each direction for a total uncertainty of .17678 in² or .00123 ft². The total uncertainty value for the coefficients of lift and drag for each drop can now be determined. These values are listed below in tabular form.

Table C.1 Uncertainty of Drop One

lift	10.25912
$\frac{\partial \text{lift}}{\partial \text{Weight}}$	0.683941
$\frac{\partial \text{lift}}{\partial \text{Height}}$	-0.068252
$\frac{\partial \text{lift}}{\partial x}$.0772802
uncertainty in weight	.353553
uncertainty in height	5
uncertainty in x	6.708
uncertainty in lift	6.267 percent
velocity	18.2764
$\frac{\partial \text{velocity}}{\partial \text{time}}$	-3.046071
$\frac{\partial \text{velocity}}{\partial \text{Height}}$	0.12159
$\frac{\partial \text{velocity}}{\partial x}$	0.114
uncertainty in time	.5
uncertainty in height	5
uncertainty in x	6.708
uncertainty in velocity	5.345 percent
$\frac{\partial C_L}{\partial \rho}$	-0.797
$\frac{\partial C_L}{\partial \text{velocity}}$	-0.087
$\frac{\partial C_L}{\partial \text{lift}}$	0.078
$\frac{\partial C_L}{\partial \text{span}}$	-0.027
uncertainty in ρ	0.000056
uncertainty in velocity	0.977
uncertainty in lift	0.643
uncertainty in span	0.00123
uncertainty in C_L	12.4 percent
drag	10.94306
$\frac{\partial \text{drag}}{\partial \text{Weight}}$	0.730
$\frac{\partial \text{drag}}{\partial \text{Height}}$	0.0640
$\frac{\partial \text{drag}}{\partial x}$	-0.0683
uncertainty in weight	.353553
uncertainty in height	5
uncertainty in x	6.708
uncertainty in drag	5.622 percent
$\frac{\partial C_D}{\partial \rho}$	-0.85
$\frac{\partial C_D}{\partial \text{velocity}}$	-0.0930
$\frac{\partial C_D}{\partial \text{drag}}$	0.0777
$\frac{\partial C_D}{\partial \text{span}}$	-0.0286
uncertainty in ρ	0.000056
uncertainty in velocity	0.977
uncertainty in lift	0.643
uncertainty in span	0.00123
uncertainty in C_D	12.2 percent

BIBLIOGRAPHY

- [1] Etkin, B. *Dynamics of Flight - Stability and Control*, 2nd edition, New York: Wiley, 1992.
- [2] Anderson, John D. *Introduction to Flight*, 4th edition, New York: McGraw-Hill, 2000.
- [3] Anderson, John D. *Fundamentals of Aerodynamics*, 2nd edition, New York: McGraw-Hill, 1991.
- [4] Horner, S. F. and Borst, H.V. *Fluid - Dynamic Lift* Brick Town, NJ, L.A. Horner, 1975.
- [5] Brandt, Steven A. Stiles, Randall J. Bertin, John J. Whitford Ray *Introduction to Aeronautics: A Design Perspective* Reston, VA: American Institute of Aeronautics and Astronautics, Inc, 1997.
- [6] Lissman, P. B. S., and G. J. Brown, "Apparent Mass Effects on Parafoil Dynamics," AIAA-93-1236, 1993. pp. 233-239.
- [7] Lingard, John Stephen. "Parachute Systems Technology Short Course, Aerodynamics of Gliding Parachutes," University of Minnesota, 1994.
- [8] Lingard, John Stephen. "Parachute Systems Technology Short Course, Aerodynamics II unsteady Aerodynamics" University of Minnesota, 1994.

- [9] Beckwith, Thomas G. and Marangoni, Roy D. *Mechanical Measurements*, 4th edition, Reading, Massachusetts: Addison-Wesley Publishing Company, Inc. 1990.
- [10] Tsai, Bruce Hung-I., "Analytical and Experimental Study of a Recovery Guidance System Using Vortex Lattice Method, Output Regulator and Proportional Navigation Guidance," Iowa State University 1999.
- [11] Figlio Richard S. and Beasley Donald E. *Theory and Design for Mechanical Measurements* New York: Wiley, 1991.

ACKNOWLEDGMENTS

I would like to take this opportunity to express my thanks to Dr. Haan, Dr. Vogel, Greg Leavitt, Colt Wallace, Thomas Calgaard, Zachary Chisman, and Mike Cook for all their help and advice. I would also like to thank the Aerospace Engineering department at Iowa State University, the Spacecraft System and Operation Laboratory and all those who helped with the experiments and making this research possible.